Cell Reports

Article

Tissue-Specific DNA Repair Activity of ERCC-1/XPF-1

Graphical Abstract

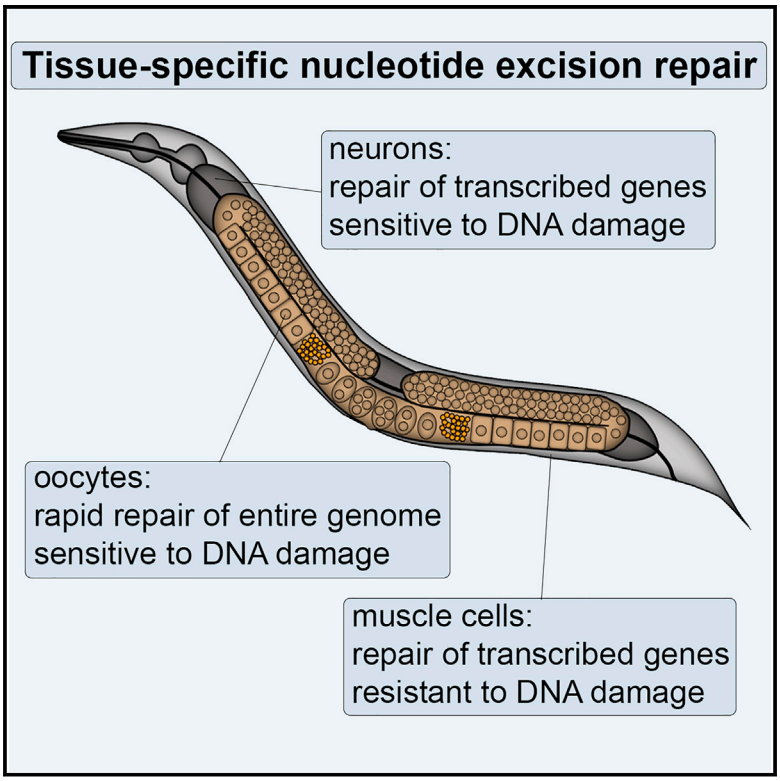

Highlights

- *In vivo* imaging shows that ERCC-1/XPF-1 exhibits tissue-specific activity
- Nucleotide excision repair provides rapid repair of the entire genome in oocytes
- Nucleotide excision repair only maintains transcribed genes in somatic cells
- Neurons are sensitive to and muscle cells are resistant to DNA damage

Authors

Mariangela Sabatella, Karen L. Thijssen, Carlota Davó-Martínez, Wim Vermeulen, Hannes Lans

Correspondence

w.vermeulen@erasmusmc.nl (W.V.), w.lans@erasmusmc.nl (H.L.)

In Brief

Sabatella et al. image the DNA repair endonuclease ERCC-1/XPF-1 in *C. elegans* to show that nucleotide excision repair exhibits tissue-specific activity. DNA lesions are very rapidly removed from the entire genome in oocytes but only from transcribed genes in somatic cells. Neurons are more sensitive to DNA damage than muscle cells.

Sabatella et al., 2021, Cell Reports *34*, 108608
January 12, 2021
https://doi.org/10.1016/j.celrep.2020.108608

CellPress

Cell Reports

CellPress
OPEN ACCESS

Article

Tissue-Specific DNA Repair Activity of ERCC-1/XPF-1

Mariangela Sabatella,[1,2] Karen L. Thijssen,[1] Carlota Davó-Martínez,[1] Wim Vermeulen,[1,*] and Hannes Lans[1,3,*]
[1]Department of Molecular Genetics, Oncode Institute, Erasmus MC, University Erasmus Medical Center Rotterdam, Dr. Molewaterplein 40, 3015 GD Rotterdam, the Netherlands
[2]Present address: Mariangela Sabatella, Princess Máxima Center for Pediatric Oncology, Heidelberglaan 25, 3584 CT Utrecht, the Netherlands
[3]Lead Contact
*Correspondence: w.vermeulen@erasmusmc.nl (W.V.), w.lans@erasmusmc.nl (H.L.)
https://doi.org/10.1016/j.celrep.2020.108608

SUMMARY

Hereditary DNA repair defects affect tissues differently, suggesting that *in vivo* cells respond differently to DNA damage. Knowledge of the DNA damage response, however, is largely based on *in vitro* and cell culture studies, and it is currently unclear whether DNA repair changes depending on the cell type. Here, we use *in vivo* imaging of the nucleotide excision repair (NER) endonuclease ERCC-1/XPF-1 in *C. elegans* to demonstrate tissue-specific NER activity. In oocytes, XPF-1 functions as part of global genome NER (GG-NER) to ensure extremely rapid removal of DNA-helix-distorting lesions throughout the genome. In contrast, in post-mitotic neurons and muscles, XPF-1 participates in NER of transcribed genes only. Strikingly, muscle cells appear more resistant to the effects of DNA damage than neurons. These results suggest a tissue-specific organization of the DNA damage response and may help to better understand pleiotropic and tissue-specific consequences of accumulating DNA damage.

INTRODUCTION

Cells continuously acquire DNA damage from exposure to environmental pollutants, radiation, and their own metabolism. DNA lesions seriously threaten health, because they interfere with genome function and lead to accumulation of mutations, causing cancer, aging, and genetic disease. The DNA damage response (DDR) is an intricate network of DNA damage repair and signaling pathways that deals with these lesions depending on their type and genomic location and the cell-cycle phase (Hoeijmakers, 2009). In addition, it is becoming increasingly clear that also the cell type and its developmental and differentiation state within an organism determine how lesions are dealt with (Lans and Vermeulen, 2015). However, most knowledge of DDR mechanisms is based on *in vitro* experimentation and/or analysis of single-cell organisms and cells in culture, and not much is known on how the DDR is organized *in vivo*.

Hereditary DNA repair pathway mutations cause different diseases characterized by cancer predisposition, developmental defects, neurodegeneration, and progeria (Keijzers et al., 2017). Typically, not all tissues are equally affected, suggesting that the DDR acts differently according to the function of each tissue (Niedernhofer, 2008). Even mutations in the same DNA repair gene can give rise to different diseases in which tissues are differently affected. A prime example is deficiency of the structure-specific endonuclease ERCC1/XPF, which plays a pivotal role in damaged-strand incision during nucleotide excision repair (NER), unhooking of interstrand crosslinks (ICLs) as part of the Fanconi anemia (FA) pathway, and removal of DNA overhangs during double-strand break (DSB) repair (Ahmad et al., 2008; Klein Douwel et al., 2014; Manandhar et al., 2015; Sijbers et al., 1996; De Silva et al., 2000). Mutations that affect ERCC1/XPF activity in NER give rise to a high incidence of skin cancers and, in some cases, progressive neurodegeneration, as observed in xeroderma pigmentosum (XP) patients (DiGiovanna and Kraemer, 2012), or to additional symptoms such as dwarfism, sensorineural impairment, and early death, as observed in Cockayne syndrome (CS) patients (Natale and Raquer, 2017). Conversely, mutations that affect ERCC1/XPF activity in ICL repair mainly give rise to hematological abnormalities and developmental failure, as observed in FA patients (Bogliolo et al., 2013). It is currently not understood why defects in the same gene, which impair different DDR pathways, cause symptoms in different tissues and whether this reflects a tissue-specific activity of the complex.

NER removes many diverse DNA-helix-distorting lesions, including those induced by UV light, i.e., cyclobutane-pyrimidine dimers (CPDs) and 6-4 pyrimidine-pyrimidone photoproducts (Lans et al., 2019; Marteijn et al., 2014). NER consists of two subpathways. Global genome NER (GG-NER) deals with damage anywhere in the genome and is initiated when damage is detected by the UV-DDB and XPC-RAD23B-CETN2 complexes, whereas transcription-coupled NER (TC-NER) specifically deals with damage that blocks transcription and is initiated by stalling of RNA polymerase II and recruitment of the CSA, CSB, and UVSSA proteins. Upon damage detection, the transcription

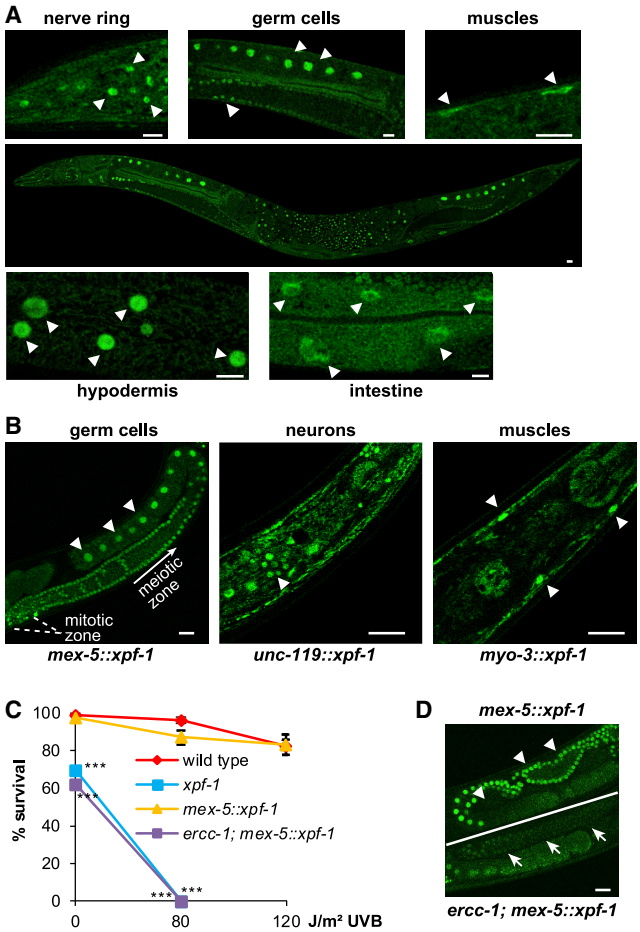

Figure 1. XPF-1::GFP Expression in *C. elegans*

(A) Representative fluorescence image of a fixed animal (middle panel) showing XPF-1::GFP expression in nuclei of multiple cell types of an *xpf-1::gfp* knockin animal. Scale bars, 10 μm. Upper and lower panels depict zoomed-in areas. Arrowheads indicate nuclei of indicated cell types.

(B) Representative pictures showing exclusive XPF-1::GFP expression in fixed adult animals in nuclei (white arrowheads) of germ cells (*mex-5::xpf-1*), neurons (*unc-119::xpf-1*), and muscles (*myo-3::xpf-1*). Scale bar, 20 μm.

(C) Germ cell and embryo survival assay after UVB irradiation of germ cells in young adult wild-type animals, *xpf-1* mutants, *xpf-1* mutants expressing XPF-1::GFP in the germline (*mex-5::xpf-1*), and *ercc-1; xpf-1* double mutants expressing XPF-1::GFP in germ cells (*ercc-1; mex-5::xpf-1*). Percentages of hatched eggs (survival) are plotted against applied UVB doses as average of eight independent experiments. Error bars represent SEM. ***$p < 0.001$ (one-way ANOVA followed by post hoc analysis by Bonferroni's test) indicates a statistically significant difference compared to wild-type for each dose.

(D) Images of living worms, showing clear expression of XPF-1::GFP in meiotic germ cells (indicated with arrowheads) of an adult animal with intact *ercc-1* (top; *mex-5::xpf-1*) and strongly reduced expression of XPF-1::GFP in meiotic cells (indicated with arrows) of an adult *ercc-1* mutant (bottom; *ercc-1; mex-5::xpf-1*). Scale bar, 20 μm.

factor TFIIH and the DNA-binding proteins XPA and RPA are recruited to unwind DNA, check for damage, and facilitate positioning of endonucleases ERCC1/XPF and XPG that excise 22–30 nt of the damaged strand flanking the lesion. DNA synthesis and ligation fill and seal the gap.

Although GG-NER and TC-NER are both active in mammalian cells in culture, their activity may not necessarily be similar in all cell types *in vivo*. For instance, *in vitro* differentiation experiments have suggested that upon terminal differentiation, cells retain the ability to repair damage in transcribed genes but lose the ability to repair lesions in non-transcribed genomic regions (Nouspikel and Hanawalt, 2002; van der Wees et al., 2007). Accordingly, pluripotent mouse embryonic stem cells (ESCs) were found to rely more on GG-NER than on TC-NER for survival upon UV irradiation, but this was reversed in embryonic fibroblasts (de Waard et al., 2008). These results suggest that there may be a cell-type-specific organization of NER *in vivo*.

To better understand tissue-specific consequences of DNA repair deficiency, it is necessary to determine how the DDR is organized *in vivo*. The nematode *C. elegans* is an ideal model organism to study *in vivo* cell-type-specific differences in DDR organization (Lans and Vermeulen, 2015). The essential role of many DDR mechanisms, including NER, is highly conserved in *C. elegans* (Lans and Vermeulen, 2011; Rieckher et al., 2018), particularly the function of ERCC-1/XPF-1 in NER and in ICL and DSB repair (Lans et al., 2013; Pontier and Tijsterman, 2009; Saito et al., 2009; Ward et al., 2007). *ercc-1* and *xpf-1* mutant animals also show features reminiscent of ERCC1/XPF deficiency in mammals, including growth arrest, developmental failure, and reduced lifespan (Gurkar et al., 2018; Jaspers et al., 2007; Lans et al., 2013; Niedernhofer et al., 2006). Moreover, previous UV survival experiments have suggested that GG-NER is the main pathway that preserves genomic integrity in germ cells and early embryos, whereas TC-NER only becomes essential for cellular function in post-mitotic somatic cells (Lans et al., 2010). However, it remains unclear to what extent these differentiation-driven changes are due to altered activity of NER itself or to differences in the way cells respond to DNA damage. Here, we show that XPF-1 exhibits a tissue-specific spatiotemporal response to UV damage suggestive of a difference between the activity of GG-NER and TC-NER in meiotic germ cells, muscles, and neurons.

RESULTS

Tissue-Specific Expression of GFP-Tagged XPF-1

We first determined the tissue distribution of the ERCC-1/XPF-1 complex by generating a knockin *C. elegans* strain expressing XPF-1 C-terminally tagged with GFP using CRISPR-Cas9-mediated homology-directed repair. Knockin animals revealed that XPF-1 is expressed ubiquitously in nuclei of different tissues, including neurons, muscles, hypodermis, and intestine, as well as germ cells and embryos (Figure 1A). To be able to study XPF-1 function in specific cell types, we stably integrated *gfp*-tagged *xpf-1* as a single-copy transgene, using MosSCI technology (Frøkjær-Jensen et al., 2008), under control of tissue-specific promoters in *xpf-1* null mutant (*tm2842)* animals (Lans et al., 2013). We generated an *xpf-1* strain expressing XPF-1::GFP driven by the *mex-5* promoter, i.e., specifically in proliferating and meiotic cells of the germline, including oocytes, and early embryo (these *xpf-1*; *P(mex-5)::xpf-1::gfp* animals are for simplicity referred to as *mex-5::xpf-1* animals). Also, we generated *xpf-1* strains expressing XPF-1::GFP driven by the

unc-119 promoter, i.e in non-proliferating neuronal cells (for simplicity, referred to as *unc-119::xpf-1* animals) or driven by the *myo-3* promoter, i.e., in muscle cells (referred to as *myo-3::xpf-1* animals) (Figure 1B). Importantly, expression levels of XPF-1::GFP in oocytes, neurons, and muscles of these single-copy transgenic strains closely matched that of GFP-tagged endogenous XPF-1 (Figures S1A and S1B). The GFP tag did not compromise XPF-1 functionality, as its germline expression rescued embryonic lethality of *xpf-1* mutants, due to a function of *xpf-1* in meiotic recombination (Saito et al., 2009), and UVB sensitivity of *xpf-1* mutant embryos, as shown by germ cell and embryo survival assays (Figure 1C). Next, we crossed *mex-5::xpf-1* animals with an *ercc-1* loss-of-function mutant strain. *ercc-1* deficiency strongly reduced expression levels of XPF-1::GFP (Figure 1D) and abolished its ability to rescue embryonic lethality and UV hypersensitivity of *xpf-1* mutant animals (Figure 1C). This shows that XPF-1 stability and functionality is dependent on its obligate complex partner, ERCC-1, as previously shown in human cells (Biggerstaff et al., 1993; Sabatella et al., 2018; van Vuuren et al., 1993), and that GFP-tagged XPF-1 is in complex with ERCC-1.

XPF-1 Protects against UVB in Oocytes and Neurons, but Not in Muscles

To study how XPF-1::GFP expression impacts NER in different tissues, we tested UV sensitivity of *mex-5::xpf-1, unc-119::xpf-1* or *myo-3::xpf-1* animals using two different survival assays. The first is the "germ cell and embryo survival assay" that measures UV survival of proliferating germ and early embryonic cells, which mostly depends on GG-NER, and found that *mex-5*-driven XPF-1::GFP rescues UV hypersensitivity of *xpf-1* embryos (Figure 1C). The second is the "L1 larvae survival assay," which measures UV sensitivity of post-mitotic somatic cells (i.e., continuation of larval development), which mostly depends on TC-NER (Lans and Vermeulen, 2011; Lans et al., 2010). *xpf-1* mutant animals are strongly UV hypersensitive in both assays, because XPF-1 is essential for GG-NER and TC-NER (Lans et al., 2013; Sijbers et al., 1996). In the germ cell and embryo survival assay, both *unc-119::xpf-1* and *myo-3::xpf-1* were as hypersensitive to UV as *xpf-1* mutant animals, in contrast to *mex-5::xpf-1* worms (Figures 1C and 2A), which was expected, because in these animals, XPF-1::GFP is not expressed in germ cells. In the L1 larvae survival assay, we surprisingly observed that only XPF-1::GFP expression in neurons (i.e., in *unc119::xpf-1* animals) rescued UV hypersensitivity of *xpf-1* mutants, but XPF-1::GFP expression in muscles (i.e., in *myo-3::xpf-1*) did not (Figure 2B). Both *unc-119* and *myo-3* promoters are active in L1 larvae (at the time of irradiation; Figure S1C) (Ardizzi and Epstein, 1987; Maduro and Pilgrim, 1995), ruling out that differences in timing of expression underlie this neuron-specific rescue. To verify this unexpected result, we transiently expressed XPF-1::GFP under control of alternative neuron (*aex-3*) and muscle (*hlh-1*) promoters by introducing *aex-3::xpf-1* and *hlh-1::xpf-1* constructs as extrachromosomal arrays in *xpf-1* mutants. Both promoters are active in larval and adult stages (Krause et al., 1990; Sassi et al., 2005), but only neuronal XPF-1 expression rescued *xpf-1* UV hypersensitivity, whereas muscle expression did not (Figure 2C). This rescue by *aex-3* driven XPF-1::GFP expression was partial likely because of the transient (and thus mosaic) expression of the transgene.

To further explore this striking difference, we tested the impact of cell-specific *xpf-1* depletion and thus NER inactivation. We fused an auxin-inducible degradation (AID) tag (Zhang et al., 2015) to XPF-1 by inserting this tag between *xpf-1* and *gfp* in the *xpf-1::gfp* knockin animals (referred to as *xpf-1::AG* animals for simplicity). Also, we generated animals expressing *Arabidopsis* TIR1 (fused to mRuby) (Zhang et al., 2015) specifically in either neurons, under control of the *unc-119* promoter (*unc-119::TIR1*), or muscles, under control of the *myo-3* promoter (*myo-3::TIR1*), and crossed these animals with *xpf-1::AG* animals. Culturing animals on auxin, which activates a TIR1 E3 ubiquitin ligase complex that ubiquitylates the AID tag, led to specific degradation of XPF-1::AID::GFP in neurons (in *xpf-1::AG; unc-119::TIR1*; Figure S1D) or muscles (in *xpf-1::AG; myo-3::TIR1*; Figure S1E). Strikingly, only XPF-1 depletion in neurons led to strong UV hypersensitivity of L1 larvae, whereas XPF-1 depletion in muscles caused only mild UV hypersensitivity (Figure 2D). As independent confirmation, we crossed *xpf-1::AG* animals with other recently generated strains expressing TIR1 (fused to mRuby) in either neurons, under control of the *rgef-1* promoter (*rgef-1::TIR1*), or muscles, under control of the *unc-54* promoter (*unc-54::TIR1)* (Ashley et al., 2020). Again, we observed that depletion of XPF-1 in neurons impeded growth of UV-irradiated larvae much stronger than depletion in muscles (Figures 2E, S1D, and S1E).

Together, these data indicate that NER activity in the germline and developing embryo suffices to rescue embryonic lethality of UV-irradiated *xpf-1*-deficient animals. Remarkably, for L1 larvae, expression of XPF-1 in neuronal cells, as opposed to expression in muscle cells, is sufficient to almost completely protect against UV hypersensitivity. These data suggest that in UV-irradiated animals, neuronal NER activity and functionality is more important than that of muscle cells.

In Oocytes, XPF-1 Quickly Repairs Damaged DNA in a GG-NER-Dependent Manner

We next investigated the *in vivo* DNA binding kinetics of XPF-1::GFP in different tissues and focused first on germ cells. *C. elegans* germ cells are arranged in a spatiotemporal gradient of differentiation in two gonad arms, which at their proximal ends harbor diakinesis-stage oocytes that are readily discernable by microscopy. In oocytes, DNA is highly condensed and organized in six pairs of homologous chromosomes (called bivalents), which allows a straightforward visualization of protein binding to DNA. To study binding of XPF-1::GFP to UV-damaged DNA in these cells, we determined its subnuclear localization in animals fixed with paraformaldehyde at different time points after UVB irradiation. We observed clear localization of XPF-1::GFP to bivalents 5 and 15 min after UV irradiation (Figure 3A), indicating that XPF-1::GFP is targeted to UV-damaged chromatin, which thus reflects active NER. Strikingly, XPF-1::GFP was redistributed throughout the whole nucleus already 30 min after UV irradiation. This fast redistribution is surprising, considering that in mammalian cells in culture, ERCC1/XPF is only redistributed from sites of UV damage after more than 4 h (Houtsmuller,

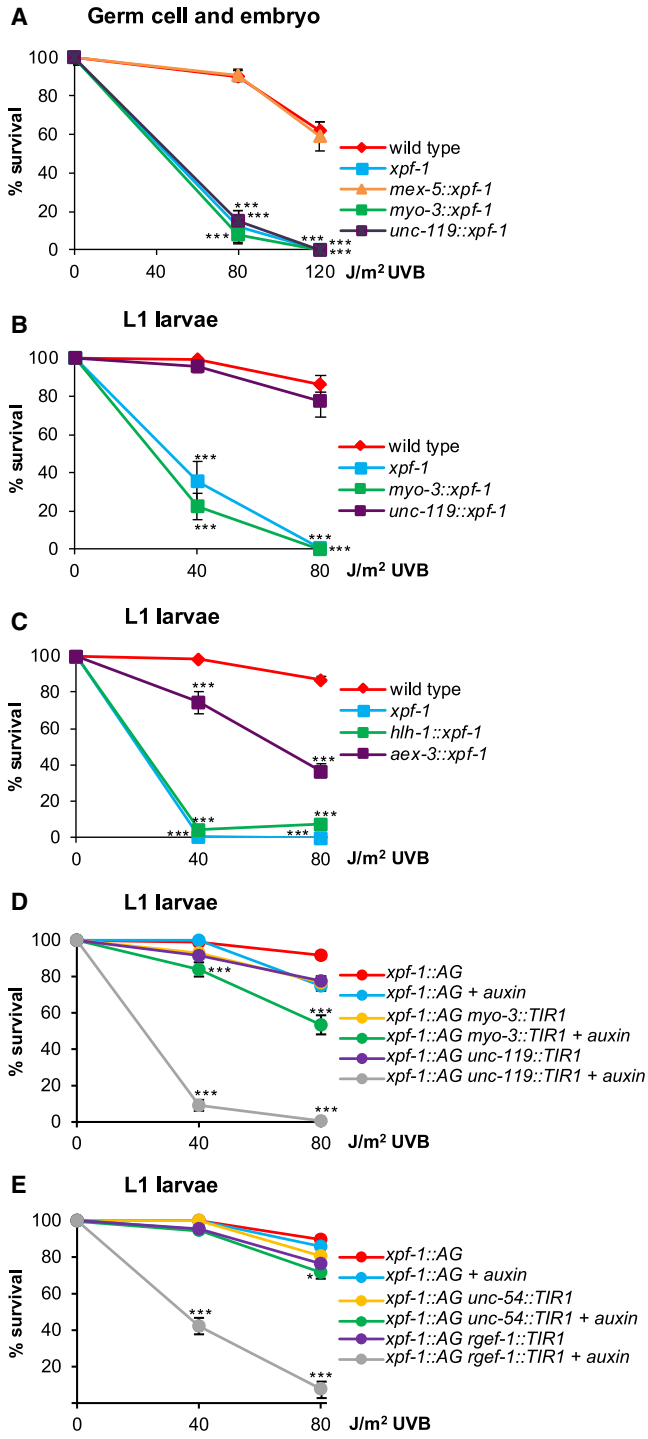

Figure 2. XPF-1 Protects against UV Irradiation in Oocytes and Neurons, but Not in Muscles

(A) Germ cell and embryo survival assay after UVB irradiation of germ cells in young adult wild-type, *xpf-1*, *mex-5::xpf-1* (germline), *myo-3::xpf-1* (muscles), and *unc-119::xpf-1* (neurons) animals. Percentages of hatched eggs (survival) after UVB irradiation are plotted against applied UVB doses. Results are plotted as average of eight independent experiments.

(B–E) L1 larvae survival assay after UVB irradiation of L1 wild-type, *xpf-1*, *myo-3::xpf-1* (muscles), and *unc-119::xpf-1* (neurons) animals (B), L1 *xpf-1* animals transiently expressing XPF-1::GFP under control of *hlh-1* (muscles) or *aex-3* (neurons) promoters (C), L1 *xpf-1::AG* animals without TIR1 or stably expressing TIR1 in muscles (*xpf-1::AG myo-3::TIR1*) or neurons (*xpf-1::AG unc-119::TIR1*) grown without or in the presence of auxin to deplete XPF-1::AG (D), and L1 *xpf-1::AG* animals without TIR1 or stably expressing TIR1 in muscles (*xpf-1::AG unc-54::TIR1*) or neurons (*xpf-1::AG rgef-1::TIR1*) grown without or in the presence of auxin to deplete XPF-1::AG (E). Percentages of animals that developed beyond the L2 stage (survival) after irradiation are plotted against applied UVB doses. Results are plotted as average of at least eight independent experiments. Error bars represent the SEM. ***p < 0.001 (one-way ANOVA followed by post hoc analysis by Bonferroni's test) indicates a statistically significant difference compared to wild-type for each dose.

1999). Indeed, immunofluorescence analysis of the recruitment of human XPF to sites of local UV damage (LUD) in U2OS cells, generated by UVC irradiation through a microporous filter, revealed that XPF was still clearly bound to damaged DNA 2 h after irradiation (Figure S2A) (Sabatella et al., 2018). To confirm the rapid XPF-1::GFP re-localization to and from UV-damaged bivalents in living oocytes, we crossed *mex-5::xpf-1* animals with worms expressing mCherry-tagged histone H2B, driven by the germline-specific *pie-1* promoter, a live-cell chromatin marker. Deconvoluted images of living oocytes closest to the uterus (−1 oocytes) showed that XPF-1::GFP is distributed throughout the nucleoplasm in untreated animals (Figure 3B). However, a clear accumulation of the protein to damaged bivalents was observed 5 and 15 min after UVB irradiation, which disappeared between 25 and 45 min after UVB irradiation.

Previously, we showed that in *C. elegans* germ cells, GG-NER, but not TC-NER, predominantly protects against UV damage (Lans et al., 2010). To show that accumulation of XPF-1::GFP on UV-damaged bivalents reflects repair by GG-NER, we crossed *mex-5::xpf-1* with *xpc-1* and *csb-1* mutants that lack functional GG-NER or TC-NER, respectively. XPF-1::GFP clearly accumulated on damaged DNA in oocytes of *csb-1* mutants, but its accumulation was mostly absent in *xpc-1* mutant oocytes (Figure 3C), indicating that XPF-1::GFP binds to bivalents mainly because of GG-NER activity. This, in combination with its relatively rapid dissociation from bivalents, may therefore suggest that GG-NER of UV photolesions in oocytes is completed within ~30 min. Such a fast repair is surprising and uncommon when compared to NER rates in human cells (Mitchell et al., 1985) or in *C. elegans* embryos, larvae, and adults (Hartman et al., 1989; Meyer et al., 2007). To test whether indeed such fast repair occurs, we measured clearance of CPDs by immunostaining of nonirradiated and UVB-irradiated wild-type and *xpf-1* oocytes with anti-CPD antibody. In wild-type *C. elegans*, CPD staining was clearly detectable on the bivalents 5 min after UV but, remarkably, was not detectable after 30 min (Figures 3D and 3E). In contrast, in *xpf-1* mutant oocytes, strong CPD staining persisted up to 2 h after UV due to lack of repair. Furthermore, CPD lesions were also still observed 2 h after UV in nuclei of wild-type mitotic germ cells at the distal tip of the gonad arm and in nuclei of early embryos (Figures S2B and S2C), indicating that in these cells, repair is slower than in oocytes. Together, these observations indicate that in irradiated *C. elegans* oocytes, XPF-1 engages in GG-NER to excise UV photolesions in an unprecedented fast manner.

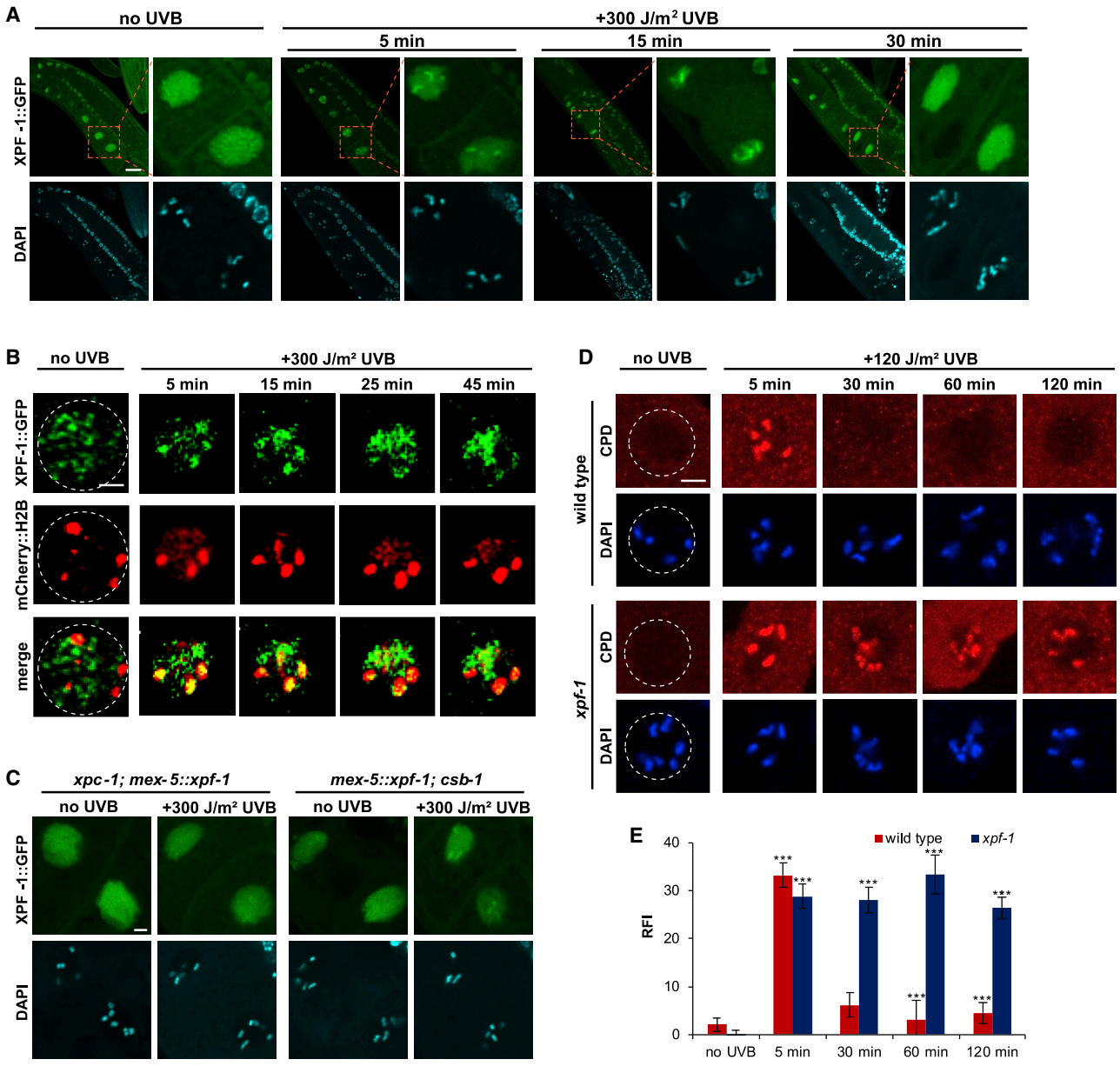

Figure 3. In Oocytes, XPF-1 Is Quickly Recruited to Damaged DNA in a GG-NER-Dependent Manner

(A) Representative pictures (with zoomed-in area) of UVB-damaged bivalent recruitment of XPF-1::GFP in oocytes of adult *mex-5::xpf-1* (germline) animals fixed without irradiation (no UVB) or fixed 5, 15, or 30 min after global irradiation with 300 J/m^2 UVB. DAPI was used as DNA marker. Scale bar, 5 μm.

(B) Deconvoluted pictures of −1 oocytes of living adult *mex-5::xpf-1* (germline) animals showing XPF-1::GFP distribution with no UVB or 5, 15, 25, and 45 min after global irradiation with 300 J/m^2 UVB. *mex-5::xpf-1* animals were crossed with animals expressing mCherry::H2B as chromatin marker. Scale bar, 5 μm. Dashed white circle represents edge of the nucleus.

(C) Representative pictures of UVB-damaged bivalent recruitment of XPF-1::GFP in oocytes of adult *xpc-1;mex-5::xpf-1* and *mex-5::xpf-1;csb-1* (germline) mutants with no UVB or 5 min after global irradiation with 300 J/m^2 UVB. DAPI was used as DNA marker. Scale bar, 5 μm.

(D) Representative immunofluorescence pictures of −1 oocytes of adult wild-type and *xpf-1* mutants with no UVB or 5, 30, 60, and 120 min after global irradiation with 120 J/m^2 UVB. Oocytes in dissected gonads were stained with CPD antibodies and DAPI as DNA marker. Scale bar, 5 μm. Dashed white circle represents edge of the nucleus.

(E) Quantification of CPD staining on bivalents as determined by immunofluorescence experiments shown in (D). CPD staining intensity, corrected for nuclear background staining, is plotted as average of at least 30 bivalents per condition from two independent experiments. RFI indicates relative fluorescence intensity. Error bars represent the SEM. ***$p < 0.001$ (one-way ANOVA followed by post hoc analysis by Bonferroni's test) indicates a statistically significant difference compared to respective untreated sample.

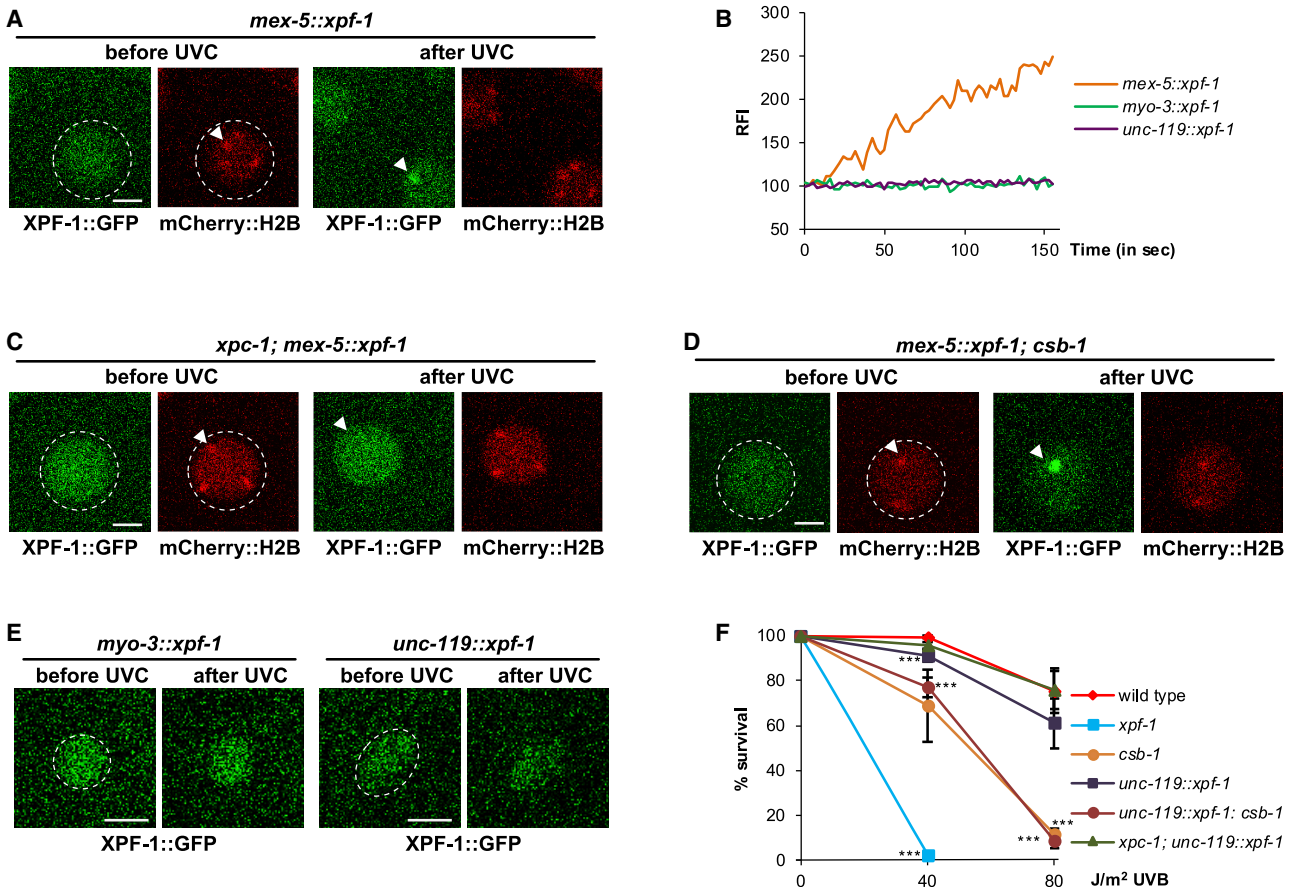

Figure 4. XPF-1 Quickly Localizes to Local UV Damage (LUD) in Oocytes, but Not in Neurons and Muscles

(A) Representative real-time imaging pictures of XPF-1::GFP recruitment to LUD in −1 oocytes of *mex-5::xpf-1* (germline) animals expressing also mCherry::H2B, before and 160 s after 266-nm UVC laser microbeam irradiation. Scale bar, 5 μm. Arrowhead indicates the bivalent on which the laser was directed. Dashed white circle represents edge of the nucleus. Shifted position of nuclei after UV is due to gonad contraction and pharyngeal pumping of the living animals. Low image resolution is due to high magnification and poor optical performance of the quartz lens needed for transmission of the UVC laser.

(B) Quantification of XPF-1::GFP recruitment to local UVC-laser-induced DNA damage, as determined by real-time imaging shown in (A) and (E). GFP fluorescence intensity at local damage sites was measured for 150 s and normalized to pre-damage values. Results are plotted as average of at least five animals per condition from at least three independent experiments. Damage was inflicted at t = 0. RFI indicates relative fluorescence intensity.

(C and D) Representative real-time imaging pictures of XPF-1::GFP recruitment to LUD in *xpc-1; mex-5::xpf-1* (C) and *mex-5::xpf-1; csb-1* (D) animals, each also expressing mCherry::H2B, before and 160 s after 266-nm laser irradiation. Scale bar, 5 μm. Arrowheads indicate the bivalents on which the laser was directed. Dashed white circle represents edge of the nucleus.

(E) Representative pictures of real-time imaging of XPF-1::GFP recruitment to LUD in body wall muscle cells of *myo-3::xpf-1* (left panel) and ventral cord neurons of *unc-119::xpf-1* (right panel) animals before and 160 s after UV damage induction. LUD was induced using 266-nm UVC laser microbeam irradiation. Scale bar, 5 μm. Dashed white circle represents the edge of the nucleus.

(F) L1 larvae survival assay after UVB irradiation of L1 wild-type, *xpf-1, csb-1* and *unc-119::xpf-1* animals and *unc-119::xpf-1; csb-1* and *xpc-1; unc-119::xpf-1* double mutants. Percentages of animals that developed beyond L2 stage (survival) after irradiation are plotted against applied UVB doses. Results are plotted as average of eight independent experiments, normalized to untreated conditions. Error bars represent SEM. ***$p < 0.001$ (one-way ANOVA followed by post hoc analysis by Bonferroni's test) indicates a statistically significant difference compared to wild-type for each dose.

XPF-1 Quickly Localizes to LUD in Oocytes, but Not in Neurons and Muscles

In nuclei of somatic cells, DNA is not organized into discernable condensed structures, making it difficult to assess XPF-1 recruitment to damaged DNA after global UV irradiation. Therefore, we optimized the use of 266-nm UVC microbeam laser irradiation (Dinant et al., 2007) to inflict subnuclear LUD in cells of adult, living *C. elegans*, immobilized using polystyrene beads on agarose pads and imaged by confocal microscopy. To validate this system, we first directed the UVC laser specifically on only one bivalent in −1 oocytes of *mex-5::xpf-1* animals. XPF-1::GFP quickly localized to UVC-laser-induced LUD, showing readily visible and quantifiable recruitment within seconds after damage infliction (Figures 4A and 4B; Video S1). Again, we observed that XPF-1::GFP recruitment mainly reflects functional GG-NER and not TC-NER, as it was absent in *xpc-1*-deficient but clearly observed in *csb-1*-deficient animals (Figures 4C and 4D; Videos S2 and S3). Moreover, this rapid accumulation suggests that GG-NER-mediated damage detection in *C. elegans* oocytes occurs relatively fast. Similar UVC-laser-

induced recruitment of human GFP-tagged XPF expressed in XPF knockout U2OS cells (Sabatella et al., 2018) shows that in human cells, XPF recruitment is initially slower and takes longer to reach a steady-state level (Figure S2D).

Next, we investigated XPF-1 recruitment to UVC-laser-induced LUD in nuclei of body wall muscle and ventral nerve cord cells, in respectively *myo-3::xpf-1* and *unc-119::xpf-1* animals, but in neither cell type did we detect XPF-1::GFP recruitment (Figures 4B and 4E). An explanation for this lack of visible recruitment could be that in these non-cycling somatic cell types, the UV response mostly relies on TC-NER. Since TC-NER only takes place in transcribed genes (i.e., in only a minor portion of the entire genome), this will require much less XPF-1 proteins at LUD than when GG-NER (i.e., in the entire genome) also takes place. Typically, in UV-irradiated human cells in culture, only ~10% of NER activity is due to TC-NER (Limsirichaikul et al., 2009), and it is therefore very hard to visualize engagement of repair proteins in this subpathway by measuring LUD recruitment (Schwertman et al., 2012). Indeed, in U2OS cells with only TC-NER activity, due to GG-NER inactivation by small interfering RNA (siRNA)-mediated XPC depletion, recruitment of human GFP-tagged XPF to LUD (induced through a microporous filter) was hardly visible (Figures S2E and S2F). Thus, similar to these siRNA-treated human cells, it is likely that the lack of visible XPF-1::GFP LUD recruitment in differentiated *C. elegans* cells is because GG-NER is not active. To verify that in neurons XPF-1 mainly acts through TC-NER, we determined if the rescued L1 larvae UV survival of *unc-119::xpf-1* animals (Figure 2B) depends on TC-NER or GG-NER by crossing these animals with *csb-1* or *xpc-1* mutants, respectively. Neuronal XPF-1::GFP expression fully rescued UV sensitivity in *xpc-1*-deficient animals, but not in *csb-1*-deficient animals (Figure 4F). Hence, XPF-1 expression in neurons protects against UV damage through its activity in TC-NER of transcribed genes.

UV-induced DNA damage inhibits transcription by physically blocking RNA polymerase II elongation, but this also leads to inhibition of transcription initiation of other, undamaged genes (Gyenis et al., 2014; Lans et al., 2019; Mayne and Lehmann, 1982; Rockx et al., 2000). TC-NER dependency therefore likely implies that UV-irradiated L1 larvae arrest development due to inhibition of transcription in neurons (Astin et al., 2008; Bianco and Schumacher, 2018; Lans and Vermeulen, 2011). Hence, to verify the importance of transcriptional integrity in neurons to larval development more directly, we generated transgenic animals expressing AID and GFP fused to the essential XPB-1 subunit of transcription initiation factor TFIIH (Schaeffer et al., 1993) by knocking in both tags at the N terminus of the *xpb-1* gene. *AID::GFP::xpb-1* animals (referred to as *AG::xpb-1* animals) were viable and without any overt phenotype, showing that the AID::GFP tag did not interfere with the essential transcription initiation function of TFIIH, and expressed fluorescent TFIIH ubiquitously, including in neurons and muscle cells (Figure S3A). Next, we crossed these animals with *unc-119::TIR1* and *myo-3::TIR1* animals to inhibit transcription in a tissue-specific manner. Similar to the L1 larvae survival assay after UV, we assessed larval development, but now in the absence or presence of auxin, causing degradation of AID::GFP::XPB-1 and thus transcription impairment in neurons (in *AG::xpb-1; unc-119::TIR1*) or muscles (in *AG::xpb-1; myo-3::TIR1;* Figure S3A). Strikingly, depletion of XPB-1 specifically in neurons, but not in muscles, of L1 larvae led to a complete growth arrest (Figure S3B), which confirms that indeed transcription cessation in neurons, either by UV irradiation in NER-deficient animals or by transcription initiation interference, leads to larval arrest.

XPF-1 Shows Tissue-Specific Mobility

To better understand the apparent difference in XPF-1 activity in oocytes, neurons, and muscle cells, we investigated XPF-1::GFP mobility, i.e., its ability to move through the nucleus, in unperturbed and UV-irradiated cells using fluorescence recovery after photobleaching (FRAP). Previous FRAP analyses have shown that human ERCC1/XPF freely diffuses through the nucleus of mammalian cells in culture but becomes partially immobilized upon UV irradiation, reflecting its incorporation into the NER pre-incision complex and binding to damaged DNA and thus its engagement in NER (Houtsmuller, 1999; Sabatella et al., 2018). Surprisingly, in unperturbed *C. elegans* cells *in vivo*, we observed only partial recovery of fluorescence in the photobleached area, suggesting that a significant fraction of XPF-1 was immobilized. Importantly, we noted mobility differences between different tissues, indicating that the fraction of proteins that (freely) diffuse through the nucleus depends on the tissue type (Figures 5A–5D). In particular, XPF-1::GFP showed the highest mobility in neurons (Figure 5D), slightly less mobility in oocytes (Figure 5A), and hardly any mobility in muscle cells (Figure 5C). As fluorescence intensity of XPF-1::GFP in muscles is comparable to that in neurons (Figures S1A and S1B), these differences are likely not caused by XPF-1 expression changes. In oocytes, XPF-1::GFP showed a clear additional UV-dependent immobilization directly after UV, indicative of its involvement in NER (Figure 5A) (Vermeulen, 2011). However, already within 10 to 20 min after UV, the XPF-1::GFP mobility returned to a level comparable to that in unperturbed cells (Figure 5B). This transient UV-induced immobilization is in line with our results suggestive of a fast repair reaction in oocytes, as lesion removal will coincide with dissociation of XPF-1::GFP from damaged DNA. In muscle cells, the already low XPF-1 mobility did not change after UV (Figure 5C), suggesting that NER might only be minimally active in this tissue. In neurons, we consistently observed a very slightly increased immobilization of XPF-1::GFP after UV irradiation (Figure 5D). This small immobilized fraction is likely derived from its engagement in repair of transcribed genes only, since NER in the entire genome does not seem to be active in these cells. Similarly, minor UV-induced immobilization in FRAP is observed in human cells for TC-NER factors (Anindya et al., 2010; van den Boom et al., 2004), but not for GG-NER factors (Hoogstraten et al., 2008). Taken together, our results suggest that ERCC1/XPF-1 displays a tissue-specific repair activity *in vivo*.

UV-Induced Transcription Block Predominantly Impairs Neuron, but Not Muscle, Integrity

To functionally validate that cells differently deal with and respond to UV-induced DNA damage, we studied the impact of UV damage and transcription blockage on neuron and muscle integrity. Previously, we have shown that germ cell

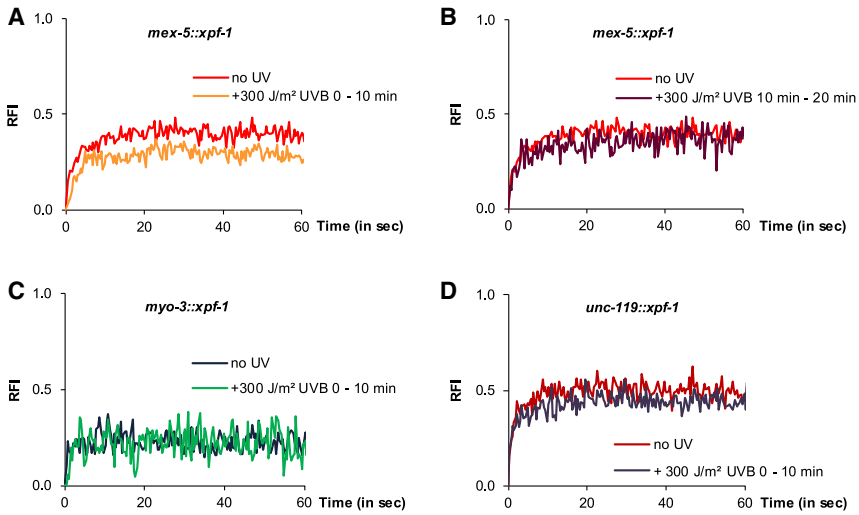

Figure 5. XPF-1 Exhibits Tissue-Specific Mobility and Damaged DNA Binding

(A–D) FRAP analysis showing XPF-1::GFP mobility in unperturbed (no UV) and UVB-irradiated (300 J/m^2) animals. FRAP was measured in a small square (explained in methods; photobleaching in the small square was optimized such that reduction in the overall nuclear fluorescence signal was minimized; Figure S4C) in nuclei of oocytes of *mex-5::xpf-1* (A and B), body wall muscle cells of *myo-3::xpf-1* (C), and ventral cord neurons of *unc-119::xpf-1* animals (D) 0–10 min or 10–20 min after irradiation, as indicated. Each curve represents average of 4–10 animals per condition from at least two independent experiments. RFI indicates relative fluorescence intensity.

integrity (i.e., meiotic maturation) is severely compromised by UV irradiation in the absence of NER (Lans et al., 2010). Here, we investigated neuron integrity by incubating nonirradiated and UV-irradiated young adult animals with the fluorescent dye DiI, which is, in unperturbed conditions, taken up by intact chemosensory amphid and phasmid neurons that contact the environment via ciliated dendrites (Hedgecock et al., 1985). Nonirradiated wild-type, *xpf-1, unc-119::xpf-1*, and *myo-3::xpf-1* animals showed clear and similar dye filling of these neurons, indicative of intact and functional cilia and dendrites (Figure 6A). Strikingly, UV irradiation strongly impaired dye filling in *xpf-1* animals, which was rescued by XPF-1::GFP reintroduction in neurons (i.e., in *unc-119::xpf-1* animals), but not in muscles. These results indicate that NER protects the integrity of neuronal cells exposed to UV irradiation. To test if this dye-filling defect is due to UV-induced transcription block in neurons, we additionally performed dye-filling experiments in *AG::xpb-1* animals expressing TIR1 in either neurons or muscles in the presence of auxin. This showed that also inhibition of transcription initiation in neurons, but not in muscles, by auxin-induced depletion of AID::GFP::XPB-1, impairs dye filling (Figure S3C). These results are consistent with the idea that UV damage functionally impairs neurons by interfering with transcription and that neuronal integrity therefore depends on TC-NER, involving XPF-1.

We investigated muscle integrity by visualizing actin filaments in sarcomeres of body wall muscle cells of nonirradiated and UV-irradiated young adult animals by staining with fluorescently labeled phalloidin (Ono and Pruyne, 2012). We did not observe striking differences in actin filament organization or muscle morphology in wild-type animals upon UV irradiation (Figure 6B). Some *xpf-1* animals showed disorganized actin filaments, but this was not systematically exacerbated by UV-induced DNA damage and unchanged by re-expression of *xpf-1* in muscles or neurons. Muscle cells appeared shortened in UV-irradiated *xpf-1* animals. However, because the whole body of these animals was shorter after UV irradiation, and because this was rescued by neuronal rather than muscle re-expression of XPF::GFP, this shortening is likely not due to DNA damage or NER deficiency in muscle cells. Next, we tested whether transcription initiation blockage by auxin-induced depletion of AID::GFP::XPB-1 led to any changes in muscle integrity or morphology, but we did not observe this (Figure S3D). Also, when *unc-119::xpf-1* L1 larvae (i.e., animals that lack functional NER in muscle cells) were UV irradiated and grown into adults, muscle cell nuclei were still readily visible by DAPI staining (Figure S4A). These results suggest that compared to neurons, muscle cells are less sensitive to the effects of UV-induced DNA damage and transcription blockage.

Finally, we investigated *C. elegans* motility, as this is dependent on properly functioning nervous and muscle systems (Gjorgjieva et al., 2014). To this end, we measured the thrashing rate (i.e., the number of lateral body movements per time unit) after UV irradiation. Whereas induction of UV damage did not affect thrashing rate of wild-type animals, *xpf-1* animals became strongly paralyzed in time after UV (Figure 6C). Strikingly, motility was almost fully rescued when XPF-1 was reexpressed in neurons but only partially when reexpressed in muscle cells. These results confirm that the deleterious consequence of unrepaired transcription-blocking UV lesions, and thus also the impact of NER deficiency, is more severe in neuronal than in muscle cell types.

C. elegans Muscle Cells Exhibit TC-NER

Finally, we studied whether TC-NER exists in muscle cells, because these cells appear largely unaffected by UV irradiation and did not show TC-NER activity by survival assays or imaging of XPF-1. It was not possible to test this by CPD immunostaining, because the fraction of CPDs removed by TC-NER is too small to be measurable. Also, standard TC-NER assays used in mammalian cell biology, such as strand-specific repair (Bohr et al., 1985) or recovery of RNA synthesis (RRS) (Mayne and Lehmann, 1982; Nakazawa et al., 2010), did not yield consistent results in our hands in *C. elegans*. Therefore, we devised an approach in which we measured recovery of protein synthesis (RPS) as readout of TC-NER. This assay is based on the same principle as the RRS assay (Mayne and Lehmann, 1982; Nakazawa et al., 2010), which is that blocked

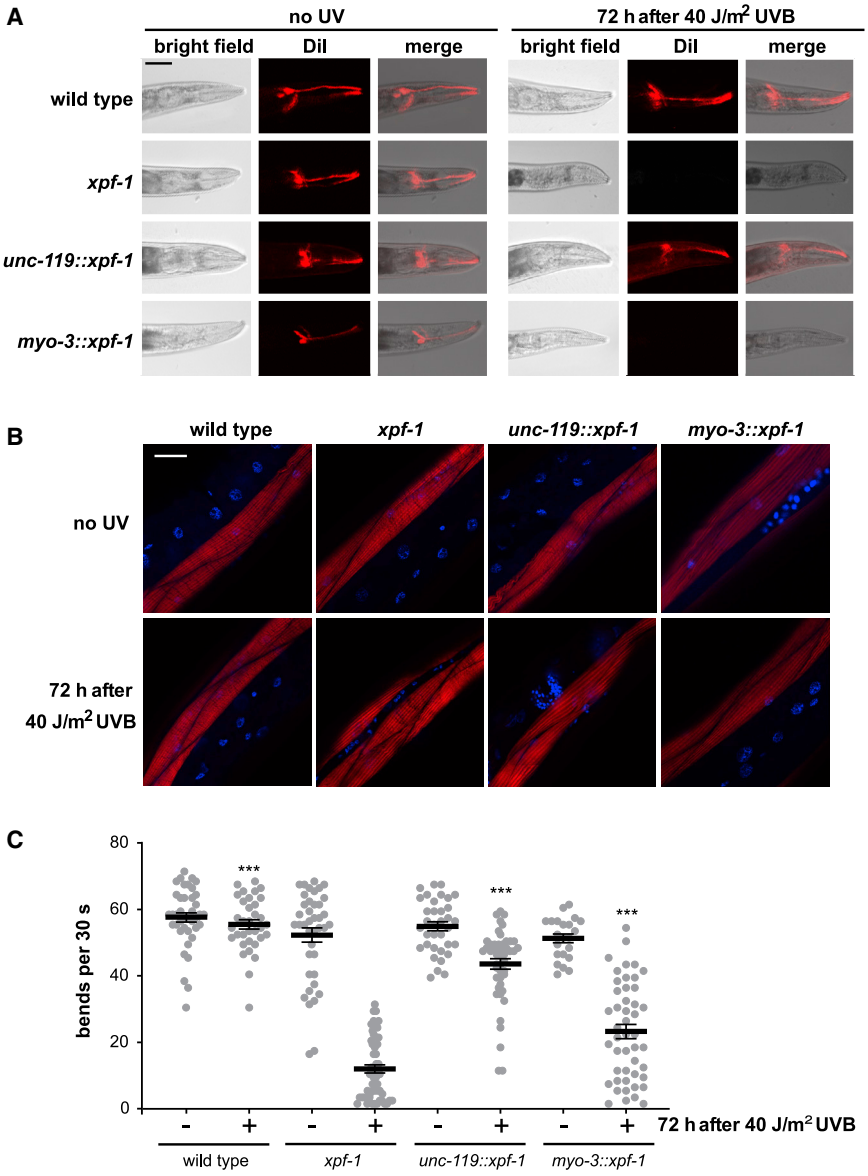

Figure 6. XPF-1 Protects Neurons against UV-Induced DNA Damage Impairment

(A) Dil dye filling (red) of wild-type, *xpf-1, unc-119::xpf-1* and *myo-3::xpf-1* adult animals, without treatment or 72 h after 40 J/m^2 UVB irradiation. Scale bar, 50 μm

(B) Phalloidin staining (red) of body wall muscles of wild-type, *xpf-1, unc-119::xpf-1*, and *myo-3::xpf-1* adult animals, without treatment or 72 h after 40 J/m^2 UVB irradiation. DNA is stained with DAPI (blue). Scale bar, 20 μm.

(C) Body bends per 30 s of wild-type, *xpf-1*, *unc-119::xpf-1*, and *myo-3::xpf-1* adult animals, without treatment or 72 h after 40 J/m2 UVB-irradiation. Shown is a scatter dot blot with mean and SEM of three independent experiments. ***p < 0.001 (one-way ANOVA followed by post hoc analysis by Bonferroni's test) indicates a statistically significant difference compared to UV-irradiated *xpf-1* animals.

transcription, and thus protein expression, is only efficiently resumed after UV irradiation if TC-NER is functional. To measure RPS, we made use of a *C. elegans* strain co-expressing AID-tagged GFP and TIR1 (fused to mRuby) in body muscle cells using the *eft-3* promoter (Zhang et al., 2015). First, we depleted GFP::AID by exposing animals to auxin, after which animals were immediately UV irradiated and allowed to recover protein synthesis. As control, animals were not exposed to auxin and/or not irradiated. Forty-eight hours after depletion, we noticed that nonirradiated NER-proficient animals had fully recovered GFP fluorescence (Figures 7A and 7B). Strikingly, while the average RPS level did not decrease after UV irradiation, with increasing UV dose, we observed a wider spread in RPS levels in individual cells. Some cells even exhibited higher GFP expression levels after UV irradiation, which could reflect a compensatory response boosting transcription after its blockage, which has been noted before (Mayne and Lehmann, 1982). Alternatively, this could be because the *eft-3* promoter is positively regulated by UV light, as the *eft-3/eef-1A.1* gene has previously been observed to be upregulated after UV irradiation (Boyd et al., 2010). In other cells, however, UV irradiation caused a clear decrease in GFP protein levels, evidencing that UV-induced DNA damage inhibited the transcription of the *GFP* gene. Next, we crossed these animals with *xpf-1* mutants to measure if RPS after UV depends on NER. Indeed, in *xpf-1* mutants we observed a wider spread in individual RPS levels and a significant decrease in the average RPS level after UV (Figures 7A and 7C). These results show that while muscle cells show only very limited XPF-1 mobility and appear largely refractory to the hazardous effects of UV damage and/or transcription inhibition, still they display TC-NER activity that is essential to overcome UV-induced transcription blockage.

DISCUSSION

C. elegans germ cells constitute an immortal and totipotent cell lineage in which the entire genome needs to be protected from DNA damage to ensure faithful transmission of genetic information to the next generation (Lans and Vermeulen, 2015). Using *in vivo* imaging, we show that in oocytes, the DNA repair activity of ERCC-1/XPF-1 fully depends on GG-NER. This is in line with previous observations by us and others that specifically GG-NER, but not TC-NER, protects against DNA-damage-induced germ cell proliferation and meiotic maturation defects and embryonic lethality (Lans and Vermeulen, 2011; Lans et al., 2010;

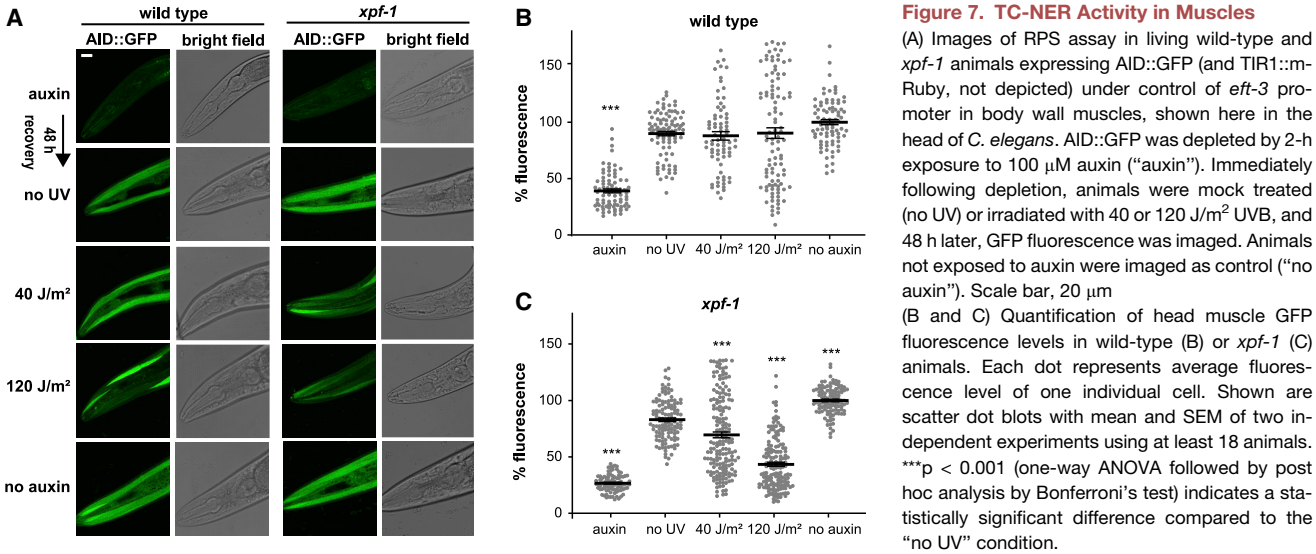

Figure 7. TC-NER Activity in Muscles

(A) Images of RPS assay in living wild-type and *xpf-1* animals expressing AID::GFP (and TIR1::mRuby, not depicted) under control of *eft-3* promoter in body wall muscles, shown here in the head of *C. elegans*. AID::GFP was depleted by 2-h exposure to 100 μM auxin ("auxin"). Immediately following depletion, animals were mock treated (no UV) or irradiated with 40 or 120 J/m^2 UVB, and 48 h later, GFP fluorescence was imaged. Animals not exposed to auxin were imaged as control ("no auxin"). Scale bar, 20 μm

(B and C) Quantification of head muscle GFP fluorescence levels in wild-type (B) or *xpf-1* (C) animals. Each dot represents average fluorescence level of one individual cell. Shown are scatter dot blots with mean and SEM of two independent experiments using at least 18 animals. ***$p < 0.001$ (one-way ANOVA followed by post hoc analysis by Bonferroni's test) indicates a statistically significant difference compared to the "no UV" condition.

Mueller et al., 2014). Importantly, we observed that in oocytes, XPF-1::GFP very quickly binds to damaged DNA, which was, surprisingly, not observed anymore 30 min after irradiation. This rapid disappearance of DNA-bound XPF coincides with the unprecedented short time it took to completely remove all UV-induced CPDs in wild-type animals, which was *xpf-1* and thus NER dependent. It should be stressed that a direct comparison of repair kinetics between different species is difficult because of the difference in genome size, the amount of lesions induced, and the type of UV light used and because of differences in the abundance of XPF and other NER proteins in cells. Still, such high repair speed contrasts to the much slower global genome CPD repair observed in yeast and human cells in culture (Mitchell et al., 1985; Sabatella et al., 2018; Teng et al., 1997) and other *C. elegans* cell types (Figures S2B and S2C) (Hartman et al., 1989; Meyer et al., 2007), which may therefore be oocyte specific. Mammalian oocytes do exhibit UV-induced unscheduled DNA repair synthesis indicative of NER (Masui and Pedersen, 1975) and are likely well able to efficiently repair many different types of DNA damage (Stringer et al., 2018), but it is unknown how fast NER operates in mammalian oocytes. Studies using UV-irradiated DNA plasmids in *Xenopus laevis* oocytes or oocyte extracts, however, which show rapid removal of CPD lesions within 1–2 h, support the idea that NER proceeds with high efficiency and speed in these types of germ cells (Adair et al., 2005; Hays et al., 1990).

It is currently unclear which mechanisms drive this unprecedented fast NER *in vivo*. Possibly, differences in chromatin conformation and/or remodeling, which impact and regulate formation and repair of UV lesions (Lans et al., 2012; Mao et al., 2017; Marteijn et al., 2014), play a role. Alternatively, the activity of GG-NER-specific NER factors such as XPC may be enhanced by oocyte-specific post-translational modifications, known to stimulate its damage detection efficiency (Marteijn et al., 2014). In *C. elegans* oocytes, 30 min is about the length of time that the proximal −1 oocyte, in which we measured XPF-1 and CPD repair kinetics, needs to mature and ovulate (McCarter et al., 1999), at which time the nuclear envelope breaks down to allow bivalents to complete diakinesis of the first meiotic prophase upon fertilization. Therefore, oocytes probably need to quickly repair damage to allow swift release of DNA-bound proteins, which may interfere with the subsequent meiotic and embryonic cell divisions, and ensure faithful transmission of undamaged genetic information. Shortly after fertilization and completion of meiosis I and II, the first embryonic cell divisions occur for which proper timing is more important than faithful genome maintenance. During this early phase of embryogenesis, the DNA damage checkpoint is suppressed and DNA damage is bypassed by translesion polymerases rather than repaired by NER (Holway et al., 2006; Roerink et al., 2012). Although this translesion synthesis allows replication to continue in the presence of DNA lesions, this process is error prone and increases the risk of mutation accumulation. Therefore, it is imperative for oocytes to be able to efficiently repair lesions and preserve genomic integrity. The higher expression of NER genes in germ cells as compared to somatic cells (Boyd et al., 2010) is a likely requisite to allow the efficient and rapid maintenance of the entire genome by GG-NER.

Contrarily to oocytes, XPF-1 expression in neurons protected L1 animals against UV irradiation in a TC-NER-dependent, but not GG-NER-dependent, manner, in line with our previous observations (Lans et al., 2010). These results suggest that somatic cells mainly focus on preserving genetic information contained in genes that are actively transcribed and needed for proper cell functionality. It was previously observed that as animals develop, the amount of UV lesions repaired in time declines and that the repair rate is highest in more actively transcribed genomic regions (Hartman et al., 1989; Meyer et al., 2007). These developmental-stage-specific changing repair activities might be explained by this differentiation-driven switch from GG-NER to TC-NER. This switch is also observed in mammalian cells, which lose their global genome repair capacity but retain repair in active genes, upon *in vitro* differentiation (Nouspikel and Hanawalt, 2002; van der Wees et al., 2007) and was suggested to

be regulated by changes in phosphorylation of the ubiquitin-activating enzyme E1 (Nouspikel and Hanawalt, 2006). Importantly, *in vivo* imaging of the spatiotemporal properties of *C. elegans* XPF-1 shows that in neurons XPF-1 behaves similarly to TC-NER factors in mammalian cells in culture; XPF-1 is not visibly recruited at LUD and only slightly immobilized upon UV irradiation in FRAP. These data exemplify the importance of TC-NER rather than GG-NER for maintaining transcriptional integrity and cell functionality in post-mitotic neurons, which likely correlates to the fact that neurodegeneration is a typical feature of human patients carrying mutations in TC-NER factors (Hoeijmakers, 2009; Karikkineth et al., 2017; Lans et al., 2019).

Our results suggest that L1 larvae arrest development upon UV irradiation due to transcription arrest, which was previously reported to involve ERK1/2 mitogen-activated protein kinase (MAPK) signaling (Astin et al., 2008; Bianco and Schumacher, 2018; Lans and Vermeulen, 2011). Considering the importance of TC-NER in somatic cells, it is striking to note that loss of *csb-1* in a wild-type or *unc-119::xpf-1* background does not completely impair UV survival of L1 larvae (Figure 4F). Apparently, XPF-1 expressed in neurons can still partially rescue UV survival in the absence of TC-NER. This can be explained by previous UV survivals showing that in somatic cells, GG-NER factors become crucial to recover UV-blocked transcription and promote L1 larvae survival when TC-NER is deficient (Babu et al., 2014; Lans et al., 2010). Thus, GG-NER is active in somatic cells but probably mainly to support the maintenance of transcribed genes. Such transcription-specific GG-NER activity has been previously described for *in-vitro*-differentiated human cell types, including neurons, and has been dubbed "transcription domain-associated repair" (Nouspikel et al., 2006; van der Wees et al., 2007). Considering that in *C. elegans* neurons, XPF-1::GFP recruitment to UVC-laser-induced UV damage is not visible, it is therefore likely that XPF-1 functions only to maintain transcribed genes, which in wild-type cells is mostly mediated by TC-NER but may also be mediated by GG-NER, as a backup system or in the absence of TC-NER.

Remarkably, we find that the activity of XPF-1, and thus that of NER, is not similar in every differentiated somatic cell type. XPF-1::GFP expression in muscles did not protect against UV irradiation as it did in neurons. Apparently, in the L1 larvae UV survival assay, which actually measures arrested development of the whole animal, the contribution of muscle cells to survival is not as important as that of neurons. Pan-neural promoters were used to drive or deplete XPF-1::GFP expression in all neurons, which in the L1 larvae make up over one-third of the animal's cells (Sulston and Horvitz, 1977). In contrast, muscle cells make up less than one-fifth of the animal's cells. Still, it is unexpected that expression of XPF-1 in only part of the animal (i.e., in neurons) is sufficient for UV survival. We also observed partial rescue of UV sensitivity when XPF-1::GFP was extrachromosomally expressed by the *lin-26* promoter, which drives specific expression in glial and hypodermal cells that make up less than one-fourth of the total amount of cells in L1 larvae (Figure S4B) (Labouesse et al., 1996). DNA damage in *C. elegans* leads to upregulation of adaptive stress and survival responses (Arczewska et al., 2013; Edifizi et al., 2017; Lans et al., 2013) and in germ cells triggers a non-cell-autonomous systemic response that promotes stress resistance of somatic cells (Ermolaeva et al., 2013). Also, persistent DNA damage in somatic cells leads to activation of the FOXO transcription factor DAF-16 that together with GATA transcription factor EGL-27 regulates and promotes development and growth (Mueller et al., 2014). It is thus conceivable that similar systemic responses to control developmental growth act in neurons (and hypodermal cells), but not in muscles.

Strikingly, in unperturbed conditions, XPF-1::GFP is less mobile in muscle cells than in oocytes or neurons or compared to mammalian cells in culture (Houtsmuller, 1999; Sabatella et al., 2018). Also, after UV irradiation, there was no measurable difference in XPF-1 mobility, in contrast to oocytes, neurons, and mammalian cells in culture. The low muscle mobility of XPF-1 is reminiscent of a similar low mobility observed for TFIIH in organotypic cultures of mouse differentiated cell types (Giglia-Mari et al., 2009) and is therefore suggestive of a tissue-specific differential organization of NER *in vivo*. This is in line with multiple studies that have addressed repair capacity in differentiated rodent muscle cell types showing a decrease in repair capacity upon differentiation (Ho and Hanawalt, 1991; Lampidis and Schaiberger, 1975). We observed that UV irradiation, even in the absence of NER, does not strongly affect muscle integrity or function in *C. elegans*, in stark contrast to its effect on neurons. Thus, our observations could indicate that genome maintenance is less important in muscles, even though our RPS assay suggests that TC-NER exists in these cells. This possibly correlates to the fact that in humans, TC-NER deficiency has a less negative impact on the muscle system than on the nervous system and that even CS symptoms displayed in the musculoskeletal system derive from denervation myopathy and disuse atrophy rather than from a direct dysfunction of muscle tissue itself (Karikkineth et al., 2017).

In summary, we conclude that NER displays tissue-specific activity, which may explain the differential impact of DNA lesions on different tissues. It will be interesting to determine if similar tissue-specific repair activities are also present in tissues of higher organisms *in vivo* and whether these can explain part of the tissue-specific symptoms associated with hereditary NER deficiency.

STAR★METHODS

Detailed methods are provided in the online version of this paper and include the following:

- KEY RESOURCES TABLE
- RESOURCE AVAILABILITY
  - Lead Contact
  - Materials Availability
  - Data and Code Availability
- EXPERIMENTAL MODEL AND SUBJECT DETAILS
- METHOD DETAILS
  - *C. elegans* strains
  - DNA repair survival assays
  - CPD immunofluorescence and imaging of fixed animals
  - Real-time imaging and FRAP in *C. elegans*

- Recovery of protein synthesis
- Dye filling
- Phalloidin staining
- Body bends measurement
- Human cell culture and siRNA
- Real-time imaging in human cells
- Immunofluorescence in human cells

- QUANTIFICATION AND STATISTICAL ANALYSIS

SUPPLEMENTAL INFORMATION

Supplemental Information can be found online at https://doi.org/10.1016/j.celrep.2020.108608.

ACKNOWLEDGMENTS

We thank Dr. G. Jansen for an injection microscope and reagents; Dr. M. Boxem, Dr. B. Goldstein, Dr. J. Ahringer, Dr. G. Seydoux, and Dr. A. Dernburg for plasmids; Dr. H. Lee and Dr. J. Ward for strains; and Dr. G. van Cappellen and the Erasmus MC Optical Imaging Center for microscope support. Some strains were provided by the *Caenorhabditis* Genetics Center (funded by NIH Office of Research Infrastructure Programs P40 OD010440) and the National Bioresource Project for the nematode. This work was supported by the Marie Curie Initial Training Network "aDDRess" funded by the European Commission 7th Framework Programme (316390), the European Research Council (advanced grant 340988-ERC-ID), the Netherlands Organization for Scientific Research (ALWOP.494 and 711.018.007), and the gravitation program CancerGenomiCs.nl from the Netherlands Organization for Scientific Research. Oncode Institute is partly financed by the Dutch Cancer Society.

AUTHOR CONTRIBUTIONS

All authors contributed ideas and designed experiments. M.S., K.L.T., C.D.-M., and H.L. performed experiments. M.S., W.V., and H.L. wrote the manuscript.

DECLARATION OF INTERESTS

The authors declare no competing interests.

Received: March 3, 2020
Revised: October 30, 2020
Accepted: December 15, 2020
Published: January 12, 2021

REFERENCES

Adair, J.E., Kwon, Y., Dement, G.A., Smerdon, M.J., and Reeves, R. (2005). Inhibition of nucleotide excision repair by high mobility group protein HMGA1. J. Biol. Chem. *280*, 32184–32192.

Ahmad, A., Robinson, A.R., Duensing, A., van Drunen, E., Beverloo, H.B., Weisberg, D.B., Hasty, P., Hoeijmakers, J.H.J., and Niedernhofer, L.J. (2008). ERCC1-XPF endonuclease facilitates DNA double-strand break repair. Mol. Cell. Biol. *28*, 5082–5092.

Anindya, R., Mari, P.O., Kristensen, U., Kool, H., Giglia-Mari, G., Mullenders, L.H., Fousteri, M., Vermeulen, W., Egly, J.M., and Svejstrup, J.Q. (2010). A ubiquitin-binding domain in Cockayne syndrome B required for transcription-coupled nucleotide excision repair. Mol. Cell *38*, 637–648.

Arczewska, K.D., Tomazella, G.G., Lindvall, J.M., Kassahun, H., Maglioni, S., Torgovnick, A., Henriksson, J., Matilainen, O., Marquis, B.J., Nelson, B.C., et al. (2013). Active transcriptomic and proteomic reprogramming in the C. elegans nucleotide excision repair mutant xpa-1. Nucleic Acids Res. *41*, 5368–5381.

Ardizzi, J.P., and Epstein, H.F. (1987). Immunochemical localization of myosin heavy chain isoforms and paramyosin in developmentally and structurally diverse muscle cell types of the nematode Caenorhabditis elegans. J. Cell Biol. *105*, 2763–2770.

Ashley, G., Duong, T., Levenson, M.T.Q., Martinez, M.A., Hibshman, J.D., Saeger, H.N., Doonan, R., Palmisano, N.J., Martinez-Mendez, R., Davidson, B., et al. (2020). Expanding the Caenorhabditis elegans auxin-inducible degron system toolkit with 1 internal expression and degradation controls and improved modular constructs for 2 CRISPR/Cas9-mediated genome editing 3. BioRxiv, 2020.05.12.090217.

Astin, J.W., O'Neil, N.J., and Kuwabara, P.E. (2008). Nucleotide excision repair and the degradation of RNA pol II by the Caenorhabditis elegans XPA and Rsp5 orthologues, RAD-3 and WWP-1. DNA Repair (Amst.) *7*, 267–280.

Aydin, Ö.Z., Marteijn, J.A., Ribeiro-Silva, C., Rodríguez López, A., Wijgers, N., Smeenk, G., van Attikum, H., Poot, R.A., Vermeulen, W., and Lans, H. (2014). Human ISWI complexes are targeted by SMARCA5 ATPase and SLIDE domains to help resolve lesion-stalled transcription. Nucleic Acids Res. *42*, 8473–8485.

Babu, V., Hofmann, K., and Schumacher, B. (2014). A C. elegans homolog of the Cockayne syndrome complementation group A gene. DNA Repair (Amst.) *24*, 57–62.

Bianco, J.N., and Schumacher, B. (2018). MPK-1/ERK pathway regulates DNA damage response during development through DAF-16/FOXO. Nucleic Acids Res. *46*, 6129–6139.

Biggerstaff, M., Szymkowski, D.E., and Wood, R.D. (1993). Co-correction of the ERCC1, ERCC4 and xeroderma pigmentosum group F DNA repair defects in vitro. EMBO J. *12*, 3685–3692.

Bogliolo, M., Schuster, B., Stoepker, C., Derkunt, B., Su, Y., Raams, A., Trujillo, J.P., Minguillón, J., Ramírez, M.J., Pujol, R., et al. (2013). Mutations in ERCC4, encoding the DNA-repair endonuclease XPF, cause Fanconi anemia. Am. J. Hum. Genet. *92*, 800–806.

Bohr, V.A., Smith, C.A., Okumoto, D.S., and Hanawalt, P.C. (1985). DNA repair in an active gene: removal of pyrimidine dimers from the DHFR gene of CHO cells is much more efficient than in the genome overall. Cell *40*, 359–369.

Boyd, W.A., Crocker, T.L., Rodriguez, A.M., Leung, M.C.K., Lehmann, D.W., Freedman, J.H., Van Houten, B., and Meyer, J.N. (2010). Nucleotide excision repair genes are expressed at low levels and are not detectably inducible in Caenorhabditis elegans somatic tissues, but their function is required for normal adult life after UVC exposure. Mutat. Res. *683*, 57–67.

Brenner, S. (1974). The genetics of Caenorhabditis elegans. Genetics *77*, 71–94.

De Silva, I.U., McHugh, P.J., Clingen, P.H., and Hartley, J.A. (2000). Defining the roles of nucleotide excision repair and recombination in the repair of DNA interstrand cross-links in mammalian cells. Mol. Cell. Biol. *20*, 7980–7990.

de Waard, H., Sonneveld, E., de Wit, J., Esveldt-van Lange, R., Hoeijmakers, J.H., Vrieling, H., and van der Horst, G.T. (2008). Cell-type-specific consequences of nucleotide excision repair deficiencies: embryonic stem cells versus fibroblasts. DNA Repair (Amst.) *7*, 1659–1669.

Dickinson, D.J., Pani, A.M., Heppert, J.K., Higgins, C.D., and Goldstein, B. (2015). Streamlined genome engineering with a self-excising drug selection cassette. Genetics *200*, 1035–1049.

DiGiovanna, J.J., and Kraemer, K.H. (2012). Shining a light on xeroderma pigmentosum. J. Invest. Dermatol. *132*, 785–796.

Dinant, C., de Jager, M., Essers, J., van Cappellen, W.A., Kanaar, R., Houtsmuller, A.B., and Vermeulen, W. (2007). Activation of multiple DNA repair pathways by sub-nuclear damage induction methods. J. Cell Sci. *120*, 2731–2740.

Edifizi, D., Nolte, H., Babu, V., Castells-Roca, L., Mueller, M.M., Brodesser, S., Krüger, M., and Schumacher, B. (2017). Multilayered reprogramming in response to persistent DNA damage in C. elegans. Cell Rep. *20*, 2026–2043.

Ermolaeva, M.A., Segref, A., Dakhovnik, A., Ou, H.L., Schneider, J.I., Utermöhlen, O., Hoppe, T., and Schumacher, B. (2013). DNA damage in germ cells induces an innate immune response that triggers systemic stress resistance. Nature *501*, 416–420.

Evans, T. (2006). Transformation and microinjection. In WormBook: The Online Review of C. elegans Biology. https://www.ncbi.nlm.nih.gov/books/NBK19648/.

Frøkjaer-Jensen, C., Davis, M.W., Hopkins, C.E., Newman, B.J., Thummel, J.M., Olesen, S.P., Grunnet, M., and Jorgensen, E.M. (2008). Single-copy insertion of transgenes in Caenorhabditis elegans. Nat. Genet. *40*, 1375–1383.

Giglia-Mari, G., Theil, A.F., Mari, P.O., Mourgues, S., Nonnekens, J., Andrieux, L.O., de Wit, J., Miquel, C., Wijgers, N., Maas, A., et al. (2009). Differentiation driven changes in the dynamic organization of Basal transcription initiation. PLoS Biol. *7*, e1000220.

Gjorgjieva, J., Biron, D., and Haspel, G. (2014). Neurobiology of *Caenorhabditis elegans* Locomotion: Where Do We Stand? Bioscience *64*, 476–486.

Gurkar, A.U., Robinson, A.R., Cui, Y., Li, X., Allani, S.K., Webster, A., Muravia, M., Fallahi, M., Weissbach, H., Robbins, P.D., et al. (2018). Dysregulation of DAF-16/FOXO3A-mediated stress responses accelerates oxidative DNA damage induced aging. Redox Biol. *18*, 191–199.

Gyenis, A., Umlauf, D., Újfaludi, Z., Boros, I., Ye, T., and Tora, L. (2014). UVB induces a genome-wide acting negative regulatory mechanism that operates at the level of transcription initiation in human cells. PLoS Genet. *10*, e1004483.

Hartman, P.S., Hevelone, J., Dwarakanath, V., and Mitchell, D.L. (1989). Excision repair of UV radiation-induced DNA damage in Caenorhabditis elegans. Genetics *122*, 379–385.

Hays, J.B., Ackerman, E.J., and Pang, Q.S. (1990). Rapid and apparently error-prone excision repair of nonreplicating UV-irradiated plasmids in Xenopus laevis oocytes. Mol. Cell. Biol. *10*, 3505–3511.

Hedgecock, E.M., Culotti, J.G., Thomson, J.N., and Perkins, L.A. (1985). Axonal guidance mutants of Caenorhabditis elegans identified by filling sensory neurons with fluorescein dyes. Dev. Biol. *111*, 158–170.

Ho, L., and Hanawalt, P.C. (1991). Gene-specific DNA repair in terminally differentiating rat myoblasts. Mutat. Res. *255*, 123–141.

Hoeijmakers, J.H.J. (2009). DNA damage, aging, and cancer. N. Engl. J. Med. *361*, 1475–1485.

Holway, A.H., Kim, S.-H., La Volpe, A., and Michael, W.M. (2006). Checkpoint silencing during the DNA damage response in Caenorhabditis elegans embryos. J. Cell Biol. *172*, 999–1008.

Hoogstraten, D., Bergink, S., Ng, J.M.Y., Verbiest, V.H.M., Luijsterburg, M.S., Geverts, B., Raams, A., Dinant, C., Hoeijmakers, J.H.J., Vermeulen, W., and Houtsmuller, A.B. (2008). Versatile DNA damage detection by the global genome nucleotide excision repair protein XPC. J. Cell Sci. *121*, 2850–2859.

Houtsmuller, A.B. (1999). Action of DNA repair endonuclease ERCC1/XPF in living cells. Science *284*, 958–961.

Iwasaki, K., Staunton, J., Saifee, O., Nonet, M., and Thomas, J.H. (1997). aex-3 encodes a novel regulator of presynaptic activity in C. elegans. Neuron *18*, 613–622.

Jaspers, N.G.J., Raams, A., Silengo, M.C., Wijgers, N., Niedernhofer, L.J., Robinson, A.R., Giglia-Mari, G., Hoogstraten, D., Kleijer, W.J., Hoeijmakers, J.H.J., and Vermeulen, W. (2007). First reported patient with human ERCC1 deficiency has cerebro-oculo-facio-skeletal syndrome with a mild defect in nucleotide excision repair and severe developmental failure. Am. J. Hum. Genet. *80*, 457–466.

Karikkineth, A.C., Scheibye-Knudsen, M., Fivenson, E., Croteau, D.L., and Bohr, V.A. (2017). Cockayne syndrome: Clinical features, model systems and pathways. Ageing Res. Rev. *33*, 3–17.

Keijzers, G., Bakula, D., and Scheibye-Knudsen, M. (2017). Monogenic diseases of DNA repair. N. Engl. J. Med. *377*, 1868–1876.

Klein Douwel, D., Boonen, R.A.C.M., Long, D.T., Szypowska, A.A., Räschle, M., Walter, J.C., and Knipscheer, P. (2014). XPF-ERCC1 acts in unhooking DNA interstrand crosslinks in cooperation with FANCD2 and FANCP/SLX4. Mol. Cell *54*, 460–471.

Krause, M., Fire, A., Harrison, S.W., Priess, J., and Weintraub, H. (1990). CeMyoD accumulation defines the body wall muscle cell fate during C. elegans embryogenesis. Cell *63*, 907–919.

Krause, M., Harrison, S.W., Xu, S.Q., Chen, L., and Fire, A. (1994). Elements regulating cell- and stage-specific expression of the C. elegans MyoD family homolog hlh-1. Dev. Biol. *166*, 133–148.

Labouesse, M., Hartwieg, E., and Horvitz, H.R. (1996). The Caenorhabditis elegans LIN-26 protein is required to specify and/or maintain all non-neuronal ectodermal cell fates. Development *122*, 2579–2588.

Lampidis, T.J., and Schaiberger, G.E. (1975). Age-related loss of DNA repair synthesis in isolated rat myocardial cells. Exp. Cell Res. *96*, 412–416.

Lans, H., and Vermeulen, W. (2011). Nucleotide excision repair in Caenorhabditis elegans. Mol. Biol. Int. *2011*, 542795.

Lans, H., and Vermeulen, W. (2015). Tissue specific response to DNA damage: C. elegans as role model. DNA Repair (Amst.) *32*, 141–148.

Lans, H., Marteijn, J.A., Schumacher, B., Hoeijmakers, J.H.J.J., Jansen, G., and Vermeulen, W. (2010). Involvement of global genome repair, transcription coupled repair, and chromatin remodeling in UV DNA damage response changes during development. PLoS Genet. *6*, e1000941.

Lans, H., Marteijn, J.A., and Vermeulen, W. (2012). ATP-dependent chromatin remodeling in the DNA-damage response. Epigenetics Chromatin *5*, 4.

Lans, H., Lindvall, J.M., Thijssen, K., Karambelas, A.E., Cupac, D., Fensgård, O., Jansen, G., Hoeijmakers, J.H.J., Nilsen, H., and Vermeulen, W. (2013). DNA damage leads to progressive replicative decline but extends the life span of long-lived mutant animals. Cell Death Differ. *20*, 1709–1718.

Lans, H., Hoeijmakers, J.H.J., Vermeulen, W., and Marteijn, J.A. (2019). The DNA damage response to transcription stress. Nat. Rev. Mol. Cell Biol. *20*, 766–784.

Limsirichaikul, S., Niimi, A., Fawcett, H., Lehmann, A., Yamashita, S., and Ogi, T. (2009). A rapid non-radioactive technique for measurement of repair synthesis in primary human fibroblasts by incorporation of ethynyl deoxyuridine (EdU). Nucleic Acids Res. *37*, e31.

Maduro, M., and Pilgrim, D. (1995). Identification and cloning of unc-119, a gene expressed in the Caenorhabditis elegans nervous system. Genetics *141*, 977–988.

Manandhar, M., Boulware, K.S., and Wood, R.D. (2015). The ERCC1 and ERCC4 (XPF) genes and gene products. Gene *569*, 153–161.

Mao, P., Wyrick, J.J., Roberts, S.A., and Smerdon, M.J. (2017). UV-induced DNA damage and mutagenesis in chromatin. Photochem. Photobiol. *93*, 216–228.

Marteijn, J.A.J.A., Lans, H., Vermeulen, W., and Hoeijmakers, J.H.J.J.H.J.J. (2014). Understanding nucleotide excision repair and its roles in cancer and ageing. Nat. Rev. Mol. Cell Biol. *15*, 465–481.

Masui, Y., and Pedersen, R.A. (1975). Ultraviolet light-induced unscheduled DNA synthesis in mouse oocytes during meiotic maturation. Nature *257*, 705–706.

Mayne, L.V., and Lehmann, A.R. (1982). Failure of RNA synthesis to recover after UV irradiation: an early defect in cells from individuals with Cockayne's syndrome and xeroderma pigmentosum. Cancer Res. *42*, 1473–1478.

McCarter, J., Bartlett, B., Dang, T., and Schedl, T. (1999). On the control of oocyte meiotic maturation and ovulation in Caenorhabditis elegans. Dev. Biol. *205*, 111–128.

Meyer, J.N., Boyd, W.A., Azzam, G.A., Haugen, A.C., Freedman, J.H., and Van Houten, B. (2007). Decline of nucleotide excision repair capacity in aging Caenorhabditis elegans. Genome Biol. *8*, R70.

Mitchell, D.L., Haipek, C.A., and Clarkson, J.M. (1985). (6-4)Photoproducts are removed from the DNA of UV-irradiated mammalian cells more efficiently than cyclobutane pyrimidine dimers. Mutat. Res. *143*, 109–112.

Mueller, M.M., Castells-Roca, L., Babu, V., Ermolaeva, M.A., Müller, R.-U., Frommolt, P., Williams, A.B., Greiss, S., Schneider, J.I., Benzing, T., et al. (2014). DAF-16/FOXO and EGL-27/GATA promote developmental growth in response to persistent somatic DNA damage. Nat. Cell Biol. *16*, 1168–1179.

Nakazawa, Y., Yamashita, S., Lehmann, A.R., and Ogi, T. (2010). A semi-automated non-radioactive system for measuring recovery of RNA synthesis and

unscheduled DNA synthesis using ethynyluracil derivatives. DNA Repair (Amst.) *9*, 506–516.

Natale, V., and Raquer, H. (2017). Xeroderma pigmentosum-Cockayne syndrome complex. Orphanet J. Rare Dis. *12*, 65.

Niedernhofer, L.J. (2008). Tissue-specific accelerated aging in nucleotide excision repair deficiency. Mech. Ageing Dev. *129*, 408–415.

Niedernhofer, L.J., Garinis, G.A., Raams, A., Lalai, A.S., Robinson, A.R., Appeldoorn, E., Odijk, H., Oostendorp, R., Ahmad, A., van Leeuwen, W., et al. (2006). A new progeroid syndrome reveals that genotoxic stress suppresses the somatotroph axis. Nature *444*, 1038–1043.

Nouspikel, T., and Hanawalt, P.C. (2002). DNA repair in terminally differentiated cells. DNA Repair (Amst). *1*, 59–75.

Nouspikel, T., and Hanawalt, P.C. (2006). Impaired nucleotide excision repair upon macrophage differentiation is corrected by E1 ubiquitin-activating enzyme. Proc. Natl. Acad. Sci. USA *103*, 16188–16193.

Nouspikel, T.P., Hyka-Nouspikel, N., and Hanawalt, P.C. (2006). Transcription domain-associated repair in human cells. Mol. Cell. Biol. *26*, 8722–8730.

Ono, S., and Pruyne, D. (2012). Biochemical and cell biological analysis of actin in the nematode Caenorhabditis elegans. Methods *56*, 11–17.

Pontier, D.B., and Tijsterman, M. (2009). A robust network of double-strand break repair pathways governs genome integrity during C. elegans development. Curr. Biol. *19*, 1384–1388.

Rieckher, M., Bujarrabal, A., Doll, M.A., Soltanmohammadi, N., and Schumacher, B. (2018). A simple answer to complex questions: Caenorhabditis elegans as an experimental model for examining the DNA damage response and disease genes. J. Cell. Physiol. *233*, 2781–2790.

Rockx, D.A.P., Mason, R., van Hoffen, A., Barton, M.C., Citterio, E., Bregman, D.B., van Zeeland, A.A., Vrieling, H., and Mullenders, L.H.F. (2000). UV-induced inhibition of transcription involves repression of transcription initiation and phosphorylation of RNA polymerase II. Proc. Natl. Acad. Sci. USA *97*, 10503–10508.

Roerink, S.F., Koole, W., Stapel, L.C., Romeijn, R.J., and Tijsterman, M. (2012). A broad requirement for TLS polymerases η and κ, and interacting sumoylation and nuclear pore proteins, in lesion bypass during C. elegans embryogenesis. PLoS Genet. *8*, e1002800.

Sabatella, M., Theil, A.F., Ribeiro-Silva, C., Slyskova, J., Thijssen, K., Voskamp, C., Lans, H., and Vermeulen, W. (2018). Repair protein persistence at DNA lesions characterizes XPF defect with Cockayne syndrome features. Nucleic Acids Res. *46*, 9563–9577.

Saito, T.T., Youds, J.L., Boulton, S.J., and Colaiácovo, M.P. (2009). Caenorhabditis elegans HIM-18/SLX-4 interacts with SLX-1 and XPF-1 and maintains genomic integrity in the germline by processing recombination intermediates. PLoS Genet. *5*, e1000735.

Sassi, H.E., Renihan, S., Spence, A.M., and Cooperstock, R.L. (2005). Gene CATCHR—gene cloning and tagging for Caenorhabditis elegans using yeast homologous recombination: a novel approach for the analysis of gene expression. Nucleic Acids Res. *33*, e163.

Schaeffer, L., Roy, R., Humbert, S., Moncollin, V., Vermeulen, W., Hoeijmakers, J., Chambon, P., and Egly, J. (1993). DNA repair helicase: a component of BTF2 (TFIIH) basic transcription factor. Science *260*, 58–63.

Schwertman, P., Lagarou, A., Dekkers, D.H.W., Raams, A., van der Hoek, A.C., Laffeber, C., Hoeijmakers, J.H.J., Demmers, J.A.A., Fousteri, M., Vermeulen, W., and Marteijn, J.A. (2012). UV-sensitive syndrome protein UVSSA recruits USP7 to regulate transcription-coupled repair. Nat. Genet. *44*, 598–602.

Sijbers, A.M., de Laat, W.L., Ariza, R.R., Biggerstaff, M., Wei, Y.F., Moggs, J.G., Carter, K.C., Shell, B.K., Evans, E., de Jong, M.C., et al. (1996). Xeroderma pigmentosum group F caused by a defect in a structure-specific DNA repair endonuclease. Cell *86*, 811–822.

Stringer, J.M., Winship, A., Liew, S.H., and Hutt, K. (2018). The capacity of oocytes for DNA repair. Cell. Mol. Life Sci. *75*, 2777–2792.

Sulston, J.E., and Horvitz, H.R. (1977). Post-embryonic cell lineages of the nematode, Caenorhabditis elegans. Dev. Biol. *56*, 110–156.

Teng, Y., Li, S., Waters, R., and Reed, S.H. (1997). Excision repair at the level of the nucleotide in the Saccharomyces cerevisiae MFA2 gene: mapping of where enhanced repair in the transcribed strand begins or ends and identification of only a partial rad16 requisite for repairing upstream control sequences. J. Mol. Biol. *267*, 324–337.

van den Boom, V., Citterio, E., Hoogstraten, D., Zotter, A., Egly, J.-M., van Cappellen, W.A., Hoeijmakers, J.H.J., Houtsmuller, A.B., and Vermeulen, W. (2004). DNA damage stabilizes interaction of CSB with the transcription elongation machinery. J. Cell Biol. *166*, 27–36.

van der Wees, C., Jansen, J., Vrieling, H., van der Laarse, A., Van Zeeland, A., and Mullenders, L. (2007). Nucleotide excision repair in differentiated cells. Mutat. Res. *614*, 16–23.

van Vuuren, A.J., Appeldoorn, E., Odijk, H., Yasui, A., Jaspers, N.G., Bootsma, D., and Hoeijmakers, J.H. (1993). Evidence for a repair enzyme complex involving ERCC1 and complementing activities of ERCC4, ERCC11 and xeroderma pigmentosum group F. EMBO J. *12*, 3693–3701.

Vermeulen, W. (2011). Dynamics of mammalian NER proteins. DNA Repair (Amst.) *10*, 760–771.

Ward, J.D., Barber, L.J., Petalcorin, M.I.R., Yanowitz, J., and Boulton, S.J. (2007). Replication blocking lesions present a unique substrate for homologous recombination. EMBO J. *26*, 3384–3396.

Zeiser, E., Frøkjær-Jensen, C., Jorgensen, E., and Ahringer, J. (2011). MosSCI and gateway compatible plasmid toolkit for constitutive and inducible expression of transgenes in the C. elegans germline. PLoS ONE *6*, e20082.

Zhang, L., Ward, J.D., Cheng, Z., and Dernburg, A.F. (2015). The auxin-inducible degradation (AID) system enables versatile conditional protein depletion in C. elegans. Development *142*, 4374–4384.

Zhang, D., Tu, S., Stubna, M., Wu, W.S., Huang, W.C., Weng, Z., and Lee, H.C. (2018). The piRNA targeting rules and the resistance to piRNA silencing in endogenous genes. Science *359*, 587–592.

STAR★METHODS

KEY RESOURCES TABLE

REAGENT or RESOURCE	SOURCE	IDENTIFIER
Antibodies		
mouse anti-CPD monoclonal antibody TDM-2	Cosmo Bio	CAC-NM-DND-001, RRID:AB_1962813
mouse anti-XPF monoclonal antibody, 3F2/3	Santa Cruz	sc-136153, RRID:AB_2098034
rabbit anti-XPC polyclonal antibody	Wim Vermeulen, this paper	N/A
rabbit anti-GFP polyclonal antibody	Abcam	ab290, RRID:AB_303395
goat anti-mouse IgG Alexa-555 antibody	Molecular probes	A21424, RRID:AB_141780
goat anti-rabbit IgG Alexa-633 antibody	Invitrogen	A-21072, RRID:AB_2535733
goat anti-rabbit IgG Alexa-555 antibody	Invitrogen	A-21429, RRID:AB_141761
goat anti-mouse IgG Alexa 488 antibody	Invitrogen	A11001, RRID:AB_2534069
Bacterial and Virus Strains		
Escherichia coli, OP50	*Caenorhabditis* Genetics Center	WormBase ID: OP50
Escherichia coli, HT115	*Caenorhabditis* Genetics Center	WormBase ID: HT115(DE3)
Chemicals, Peptides, and Recombinant Proteins		
Poly-L-lysine hydrobromide	Sigma	P1524
Vectashield with DAPI	Vector laboratories	H-1200
Polystyrene beads	Polyscience Inc	00876-15
3-indoleacetic acid	Sigma	I3750
phalloidin-Atto565	Sigma	94072
NaN_3	Sigma	S2002
DiI	Molecular Probes	D282
Experimental Models: Cell Lines		
U2OS XPF KO XPF-GFP	Sabatella et al., 2018	N/A
Experimental Models: Organisms/Strains		
C. elegans strains are listed in Table S1		N/A
Oligonucleotides		
xpf-1 crRNA ATTTCGGAAGAAAATAACAC	this paper	N/A
xpb-1 crRNA TCTTTCGTCGCCATTTCTTT	this paper	N/A
control siRNA	Dharmacon	D-001210-05
XPC siRNA CUGGAGUUUGAGACAUAUCUU	this paper	N/A
Recombinant DNA		
pJA252	Zeiser et al., 2011	RRID:Addgene #21512
pJA256	Zeiser et al., 2011	RRID:ddgene #21509
pCM5.37	Geraldine Seydoux	RRID:Addgene #17253
pLZ31	Zhang et al., 2015	RRID:Addgene #71720
pCFJ201	Zeiser et al., 2011	N/A
Software and Algorithms		
LAS AF	Leica	https://www.leica-microsystems.com/products/microscope-software/p/leica-las-x-ls/ RRID:SCR_013673
ImageJ	ImageJ	https://imagej.nih.gov/ij/, RRID:SCR_003070

(*Continued on next page*)

Continued

REAGENT or RESOURCE	SOURCE	IDENTIFIER
Graphpad Prism	GraphPad Software, Inc	https://www.graphpad.com:443/, RRID:SCR_002798
Huygens software		https://svi.nl/Huygens-Software, RRID:SCR_014237

RESOURCE AVAILABILITY

Lead Contact

Further information and requests for resources and reagents should be directed to and will be fulfilled by the Lead Contact, Hannes Lans (w.lans@erasmusmc.nl).

Materials Availability

All strains and plasmids generated in this study are available from the Lead Contact without restriction.

Data and Code Availability

This study did not generate any unique datasets or code.

EXPERIMENTAL MODEL AND SUBJECT DETAILS

All *C. elegans* strains were cultured according to standard methods (Brenner, 1974) on nematode growth media (NGM) agar plates seeded with *Escherichia coli* OP50. The wild-type strain was Bristol N2. Strains used are listed in Table S1. Developmental stages are indicated for each experiment and in the legends. Human XPF knockout osteosarcoma U2OS cells complemented with GFP-tagged XPF were previously described (Sabatella et al., 2018) and cultured in DMEM/F10 supplemented with 10% fetal calf serum (FCS) and 1% penicillin-streptomycin (PS) at 37°C and 5% CO2. U2OS cells are of female origin.

METHOD DETAILS

C. elegans strains

C. elegans was cultured according to standard methods (Brenner, 1974). The wild-type strain was Bristol N2. Mutant strains and alleles are summarized in Table S1. All mutants were backcrossed three to five times against wild-type and genotyped by PCR and sequencing. To generate *xpf-1::gfp* knockin animals, a 542 bp left and 482 bp right homology arm were amplified from wild-type genomic DNA and cloned into plasmid pDD282 (a gift from Bob Goldstein; Dickinson et al., 2015), flanking *gfp*, after which the 'self-excising cassette' was removed. To generate *aid::gfp::xpb-1* knockin animals, a gene fragment (Integrated DNA technologies) consisting of 176 bp left and 200 bp right homology arms flanking *aid::gfp* sequences was cloned into pCRII-TOPO. The plasmids were injected together with trcRNA and crRNA (targeting ATTTCGGAAGAAAATAACAC for *xpf-1* and TCTTTCGTCGCCATTTCTTT for *xpb-1*; Integrated DNA technologies) in the Cas9^{dPiRNA} expressing strain HCL67 (a kind gift from Heng-Chi Lee; Zhang et al., 2018). Knockin animals were verified by genotyping PCR and sequencing, after which the Cas9 was removed by backcrossing against wild-type.

To generate strains stably expressing XPF-1::GFP or TIR1::mRuby under control of tissue-specific promoters *mex-5*, *unc-119, myo-3 and lin26,* the MosSCI technology (Frøkjær-Jensen et al., 2008) was used. For transient XPF-1::GFP expression under control of the *aex-3* and *hlh-1* promoters, transgenes were expressed as extrachromosomal arrays (Evans, 2006). Promoter fragments of *unc-119* and *aex-3* (to drive expression in neurons; Iwasaki et al., 1997; Maduro and Pilgrim, 1995), *myo-3* and *hlh-1* (to drive expression in muscles; Ardizzi and Epstein, 1987; Krause et al., 1994), *lin-26* (to drive expression in hypodermis; Labouesse et al., 1996) were PCR amplified from wild-type genomic DNA (*myo-3*: 2499 bp upstream of ATG, *unc-119*: 2194 bp upstream of ATG, *hlh-1*: 3116 bp upstream of ATG, *aex-3*: 1343 bp upstream of ATG and *lin-26*: 3740 bp upstream of ATG) and recombined into pDONRP4-P1R using BP clonase (Invitrogen). For the *mex-5* promoter (driving expression in germ cells) and *gfp::ttb-2* sequence and 3′UTR, entry vectors pJA252 and pJA256 were used, respectively (gifts from Julie Ahringer) (Zeiser et al., 2011). For *unc-54* 3′UTR sequences *pCM5.37* was used (a gift from Geraldine Seydoux). *xpf-1* cDNA was generated by PCR amplification of wild-type cDNA and TIR1::mRuby was amplified from vector pLZ31 (a gift from Abby Dernburg) (Zhang et al., 2015) and both were cloned into pDONR221. To generate expression vectors, promoter entry vectors, *xpf-1* or TIR1::mRuby vectors and *gfp::ttb-2* or *unc-54* vectors were recombined with plasmid pCFJ201(Zeiser et al., 2011) using LR clonase II (Invitrogen). Resulting vectors were verified by sequencing. For transient expression, constructs were injected into *xpf-1(tm2842)II* animals together with either *myo-2::mCherry* or *myo-3::mCherry and elt-2::mCherry,* to maintain transgenic animals by selection for red fluorescence. For stable expression, the constructs were injected in the MosSCI strain EG6250 to generate transgenic worms which were selected after heat shock based on rescue of the *unc-119* phenotype and genotyping. All strains were backcrossed against *xpf-1(tm2842)II* or wild-type animals.

DNA repair survival assays

Germ cell and embryo survival assays were performed as previously described (Lans et al., 2010). Briefly, staged young adults were washed and irradiated on empty agar plates at the indicated UVB dose (Philips TL-12 tubes, 40W). Following a 24 h recovery period on OP50 bacteria, three to five adults were allowed to lay eggs for 3 h on 6 cm plates seeded with HT115 bacteria, in quadruple for each UVB dose. 24 h later, the amount of hatched and unhatched (dead) eggs was counted and survival percentage calculated. Results are plotted as average of at least eight independent experiments. Statistical difference was calculated using a one-way ANOVA followed by post hoc analysis by Bonferroni's test. L1 larvae survival assays were performed as previously described (Lans et al., 2010). Briefly, eggs collected from adult animals after hypochlorite treatment were plated onto agar plates seeded with HT115 bacteria, and, when indicated containing 1 mM auxin (3-indoleacetic acid, Sigma), in quadruple for each UV dose. 16 h later, L1 larvae were irradiated at the indicated doses of UVB (Philips TL-12 tubes, 40 W) and allowed to recover for 48 h. Animals arrested at the L1/L2 stages and surviving animals that developed beyond the L2 stage were counted to determine the survival percentage. During all assays, animals were kept at 20°C. Results are plotted as average of at least eight independent experiments. Statistical difference was calculated using a one-way ANOVA followed by post hoc analysis by Bonferroni's test.

CPD immunofluorescence and imaging of fixed animals

To image XPF-1::GFP in fixed animals, unperturbed or irradiated (using two Philips TL-12 tubes, 40 W, emitting UVB) adults were fixed on Poly-L-lysine hydrobromide (Sigma) slides with 4% paraformaldehyde in PBS and slides were mounted using Vectashield with DAPI (Vector laboratories). To visualize CPDs lesions, adult animals were dissected by cutting heads and tails, exposing gonads and embryos which were freeze cracked and incubated in cold methanol. Upon fixation in 4% formaldehyde in PBS, gonads were blocked with PBS containing 0.5% BSA and 0.1% Tween and incubated with 0.07 M NaOH to denature DNA. Next, gonads were incubated with CPD antibody (TDM-2; Cosmobio) overnight and with Alexa555-conjugated secondary antibody (Invitrogen) for 2 h.DAPI Vectashield (Vector Laboratories) was used to mount coverslips. Animals and oocytes were imaged using a Zeiss LSM700 confocal microscope equipped with a 40x Plan-apochromat 1.3 NA oil immersion lens (Carl Zeiss). Fluorescence intensity of the CPD staining was quantified in at least 30 bivalents/condition in two independent experiments using ImageJ software. Statistical difference was calculated using a one-way ANOVA followed by post hoc analysis by Bonferroni's test.

Real-time imaging and FRAP in *C. elegans*

To generate images of XPF-1::GFP or GFP in living animals, animals were mounted on 2% agar pads in M9 containing 10 mM NaN_3 (Sigma) and imaged on a Zeiss LSM700 or Leica SP8 confocal microscope. For measurements on XPF-1::GFP in living animals, adults were immobilized in a mix of M9 buffer and polystyrene beads (Polyscience Inc.) on 6% agarose pads on microscope slides. When indicated, adults were irradiated with 300 J/m^2 UVB (Philips TL-12 tubes, 40 W) on coverslips. After mounting of coverslips on microscope slides, animals were imaged using a Leica TCS SP5 (Leica Microsystems) or a Zeiss LSM700 confocal microscope. To perform FRAP, nuclei of oocytes, neurons and muscles were imaged at 700 Hz every 37 ms using a 488 nm laser at low power until steady-state levels were reached. Next, GFP-derived fluorescence in a small square (0.8 × 0.8 μm on a bivalent in oocytes; 0.3 × 0.3 μm for neurons and muscles, zoom 9) was photobleached using high (80%–100%) laser power. Photobleaching in the small square was optimized such that reduction in the overall nuclear fluorescence signal was minimized. Recovery of the fluorescence signal was measured at low laser power every 37 ms until steady-state levels were reached. In oocytes, the bivalent position was tracked by simultaneous imaging of mCherry::H2B using a 561 nm laser. Fluorescent signals were normalized to the average fluorescence intensity before bleaching and bleach depth and plotted as average of at least 12 animals per condition, except for oocytes between 10 and 20 min after UV for which 5 animals were averaged. For real-time imaging of XPF-1::GFP LUD recruitment, nuclei in immobilized animals were imaged using a 100x quartz objective coupled to a Leica TCS SP5 confocal microscope. Local DNA damage was inflicted using a UVC laser (266 nm, Rapp OptoElectronic, Hamburg GmbH) as previously described (Aydin et al., 2014). In oocytes, the UVC laser was specifically directed on one of the bivalents. Fluorescence intensities at sites of local damage were normalized to average fluorescence intensities before irradiation and plotted as average of at least 5 animals per condition from two independent experiments. All real-time imaging was performed at room temperature. LAS AF software (Leica) was used for imaging and ImageJ software to compensate for movement of cells and for quantification. Deconvoluted images of −1 oocytes in living animals were generated using The Huygens software.

Recovery of protein synthesis

To measure recovery of protein synthesis after UV, as readout for TC-NER, we first depleted AID::GFP (which is co-expressed with TIR1 in muscle cells by the same *eft-3* promoter), in staged L4 animals, by culturing animals for 2 h on NGM plates containing 100 μM auxin (3-indoleacetic acid, Sigma). The level of depletion was determined by measuring GFP fluorescence in body wall muscle cells in the head of living animals on a Leica SP8 confocal microscope. Directly after auxin exposure, animals were UV-irradiated with 40 or 120 J/m^2 and, together with control animals not exposed to auxin or not irradiated, cultured on NGM plates. After 48 h, the level of protein synthesis (recovery) for each condition was determined by imaging GFP fluorescence in head muscle cells of living animals.

Dye filling

For dye filling (Hedgecock et al., 1985), staged first day adult animals were mock treated or UV-irradiated (40 J/m^2 UVB) and grown for 72 h (Figure 6A) or grown 7 days in the absence or presence of 1 mM auxin (3-indoleacetic acid, Sigma; Figure S3C), as indicated.

Animals were washed and incubated for 30 min in 10 μg/ml DiI (Molecular probes) dissolved in M9 buffer. Next, animals were allowed to recover for at least 1 h on culture plates. Animals were imaged using a Leica TCS SP5 confocal microscope.

Phalloidin staining

For phalloidin staining, staged first day adult animals were mock treated or UV-irradiated (40 J/m^2 UVB) and grown for 72 h before fixation (Figure 6B) or grown for 72 h or 9 days in the absence or presence of 1 mM auxin (3-indoleacetic acid, Sigma) before fixation (Figure S3D), as indicated. To visualize actin filament organization (Ono and Pruyne, 2012), animals were fixed in 4% formaldehyde dissolved in CSK-buffer (10 mM PIPES, pH 6.1, 138 mM KCl, 3 mM $MgCl_2$, 2 mM EGTA) containing 0.32 M sucrose and permeabilized for 5 min in acetone at −20°C. Animals were stained for 30 min with 0.2 μg/ml phalloidin-Atto565 (Sigma), washed and mounted using DAPI Vectashield (Vector Laboratories). Animals were imaged using a Zeiss LSM700 confocal microscope.

Body bends measurement

To determine thrashing rate, staged first day adult animals were mock treated or UV-irradiated (40 J/m^2 UVB) and grown for 72 h (Figure 6C), after which animals were placed in 5 μl M9 buffer and allowed to acclimatize for 30 s before number of body bends was counted for 30 s.

Human cell culture and siRNA

Human XPF knockout osteosarcoma U2OS cells complemented with GFP-tagged XPF were previously described (Sabatella et al., 2018) and cultured in DMEM/F10 supplemented with 10% fetal calf serum (FCS) and 1% penicillin-streptomycin (PS) at 37°C and 5% CO_2. For siRNA treatment, cells were transfected using RNAiMax (Invitrogen) with control siRNA (Dharmacon, D-001210-05) or siRNA targeting XPC (custom, CUGGAGUUUGAGACAUAUCUU), 48 h before UVC treatment.

Real-time imaging in human cells

To measure XPF-GFP recruitment to laser induced LUD in human cells, XPF-GFP expressing cells were seeded on coverslips and imaged using a 100x quartz objective coupled to a Leica TCS SP5 confocal microscope. Local DNA damage was inflicted using a UVC laser (266 nm, Rapp OptoElectronic, Hamburg GmbH) as previously described (Aydin et al., 2014). Fluorescence intensity at sites of local damage was normalized to the average fluorescence intensity before irradiation. Results are plotted as average of at least 10 cells from two independent experiments. During imaging, cells were kept in culture medium at 37°C and 5% CO_2. LAS AF software (Leica) was used for imaging and ImageJ software for quantification.

Immunofluorescence in human cells

For immunofluorescence, human cells were seeded on coverslips and irradiated with 60 J/m^2 (254 nm UVC lamp, Philips) through an 8 μm microporous filter (Millipore) to create LUD. Cells were fixed at the indicated times after irradiation with 2% paraformaldehyde and 0.1% Triton X-100 in PBS, and permeabilized for 20 min with 0.1% Triton X-100 in PBS. DNA was denatured with 0.07 M NaOH in PBS for 5 min. PBS containing 0.15% glycine and 0.5% BSA was used to wash cells prior to 2 h incubation with primary antibodies and 1 h incubation with secondary antibodies conjugated to Alexa Fluor 488, 555 and 633 (Invitrogen). DAPI Vectashield (Vector Laboratories) was used to mount the coverslips that were subsequently imaged using a Zeiss LSM700 microscope equipped with a 40x Plan-apochromat 1.3 NA oil immersion lens (Carl Zeiss). Primary antibodies used were anti-XPF (3F2/3, Santa Cruz), anti-XPC (homemade fraction 5), anti-GFP (ab290, Abcam), anti-CPD (TDM-2; Cosmobio). Accumulation of XPF at sites of damage was measured in at least 100 cells per condition in two independent experiments.

QUANTIFICATION AND STATISTICAL ANALYSIS

The number of samples and biological replicates analyzed for each experiment are indicated in the legends. Statistical differences were calculated in GraphPad Prism software using a one-way ANOVA followed by post hoc analysis by Bonferroni's test, as indicated in the legends for each experiment.

Cell Reports, Volume *34*

Supplemental Information

Tissue-Specific DNA Repair Activity of ERCC-1/XPF-1

Mariangela Sabatella, Karen L. Thijssen, Carlota Davó-Martínez, Wim Vermeulen, and Hannes Lans

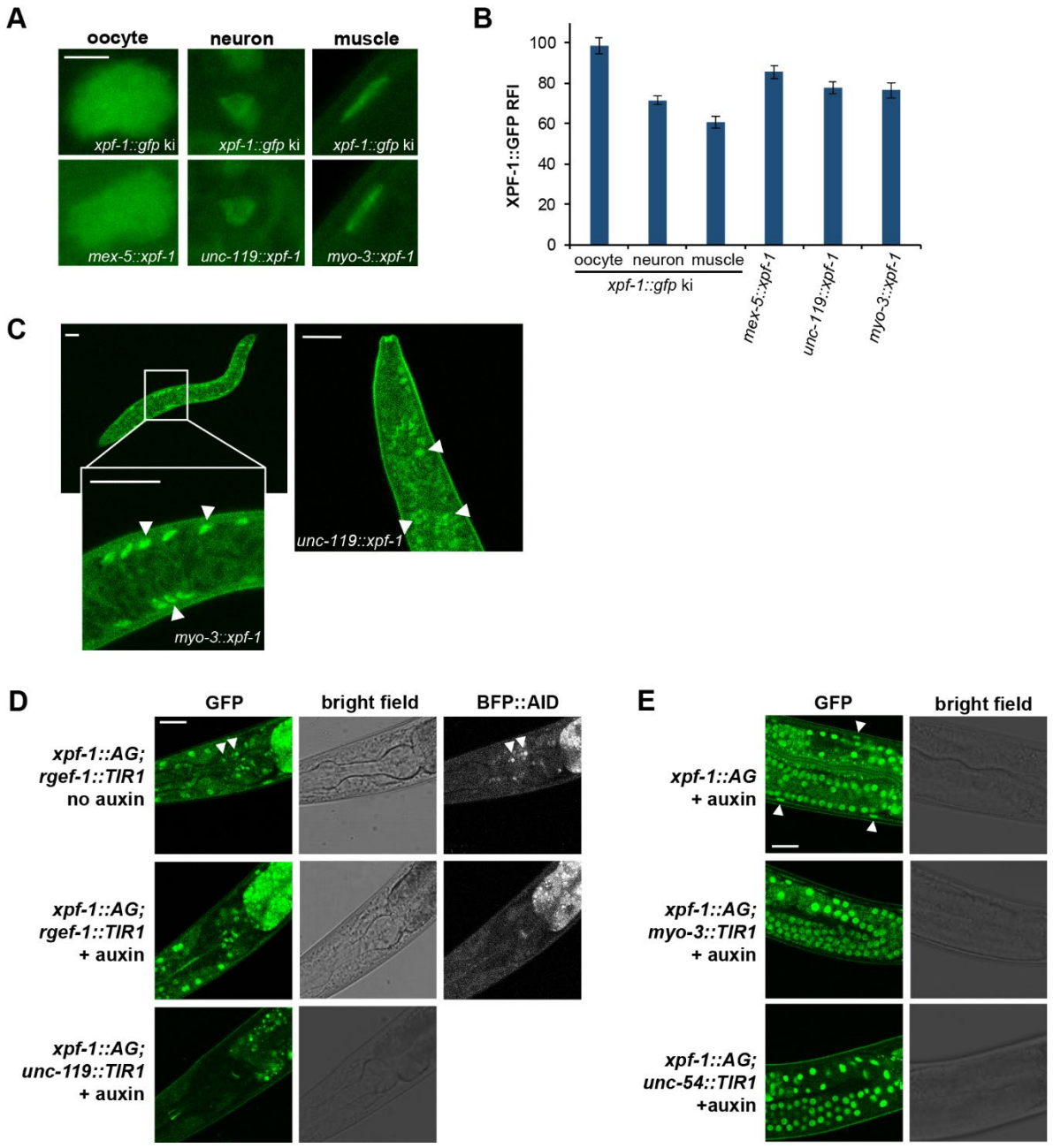

Figure S1. XPF-1 fluorescence intensities and cell-specific depletion. Related to Figures 1 and 2. (A) Representative images of XPF-1::GFP fluorescence intensities in oocytes, head neurons and body wall muscle cells in *xpf-1::gfp* knock-in (ki) and in *mex-5::xpf-1, unc-119::xpf-1* and *myo-3::xpf-1* animals. Scale bar: 5 µm. (B) Quantification of XPF-1::GFP fluorescence intensities in cells as depicted in (A). Shown is the average (+/- SEM) of at least 13 cells in at least four animals. (C) Representative images showing expression of XPF-1::GFP in nuclei (examples indicated with arrowheads) of muscles (*myo-3::xpf-1*) and head neurons (*unc-119::xpf-1*) in L1 larvae. Scale bar: 10 µm. (D) Representative images showing AID::GFP-tagged XPF-1 fluorescence in head neurons (indicated by arrowheads) in animals expressing also TIR1 (fused to mRuby, not depicted) under control of the neuronal *rgef1* (upper and middle panel) or *unc-119* promoter (bottom panel), in the absence or presence of auxin. Animals expressing TIR1 under control of the *rgef-1* promoter also express blue fluorescent AID-tagged TagBFP2 (shown with 'BFP::AID'), which like XPF-1 is also depleted from neuronal cells in the presence of auxin. Scale bar: 20 µm. (E) Representative images showing AID::GFP-tagged XPF-1 fluorescence in body wall muscle nuclei (indicated by arrowheads) of L4 *xpf-1::AG* animals grown on auxin (upper panel) and depletion of XPF-1 in these cells in animals expressing also TIR1 (fused to mRuby, not depicted) in muscles under control of either the *myo-3* (middle panel) or *unc-54* promoter (bottom panel). Scale bar: 20 µm.

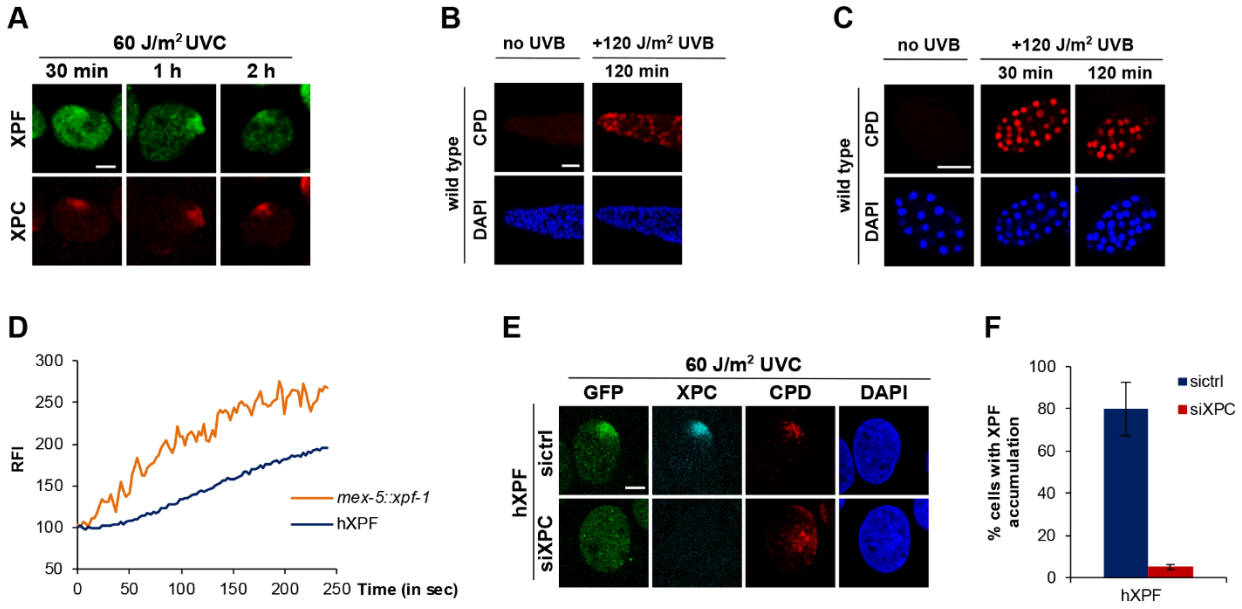

Figure S2. XPF recruitment to DNA damage and CPD repair. Related to Figures 3 and 4. (A) Representative immunofluorescence pictures of human XPF recruitment to local UV damage in U2OS cells 30 min, 1 and 2 h after irradiation with 60 J/m^2 UVC through an 8 µm microporous filter. Cells were stained with antibodies against XPF and XPC, as damage marker. Scale bar: 5 µm. (B) Representative immunofluorescence pictures of mitotic germ cells in the distal tip of dissected gonads of adult wild type animals without treatment (no UVB) or 120 min after global irradiation with 120 J/m^2 UVB. Dissected gonads were stained with antibodies against CPD photolesions and DAPI, as DNA marker. Scale bar: 5 µm. (C) Representative immunofluorescence pictures of wild type embryos without treatment (no UVB) or 30 and 120 min after global irradiation with 120 J/m^2 UVB. Embryos were stained with antibodies against CPD photolesions and DAPI, as DNA marker Scale bar: 5 µm. (D) Local UVC-laser-induced DNA damage recruitment of XPF-1::GFP in oocytes of *mex-5::xpf-1* (germ line) animals (depicted also in Figure 5B) is shown in comparison to recruitment of GFP-tagged human wild type XPF (hXPF) expressed in XPF knockout U2OS cells. GFP fluorescence intensities at sites of local damage were measured in real-time for 250 sec and normalized to pre-damage values. Results are plotted as average of at least 5 animals and 20 cells from at least two independent experiments. Damage was inflicted at t=0. (E) Representative immunofluorescence pictures of the UV damage recruitment of human XPF-GFP expressed in XPF knockout U2OS cells (hXPF) treated with non-targeting (sictrl) and XPC (siXPC) siRNAs, 1 h after irradiation with 60 J/m^2 UVC through an 8 µm microporous filter. Cells were stained with antibodies against XPC and CPD, as damage marker. Scale bar: 5 µm. (F) Percentage of cells showing clear co-localization of XPF-GFP and CPD in cells treated with non-targeting (sicntrl) and XPC (siXPC) siRNAs, as determined by immunofluorescence experiments shown in (E). Results are plotted as average of at least 190 cells from two independent experiments. RFI indicates relative fluorescence intensity. Error bars represent the SEM.

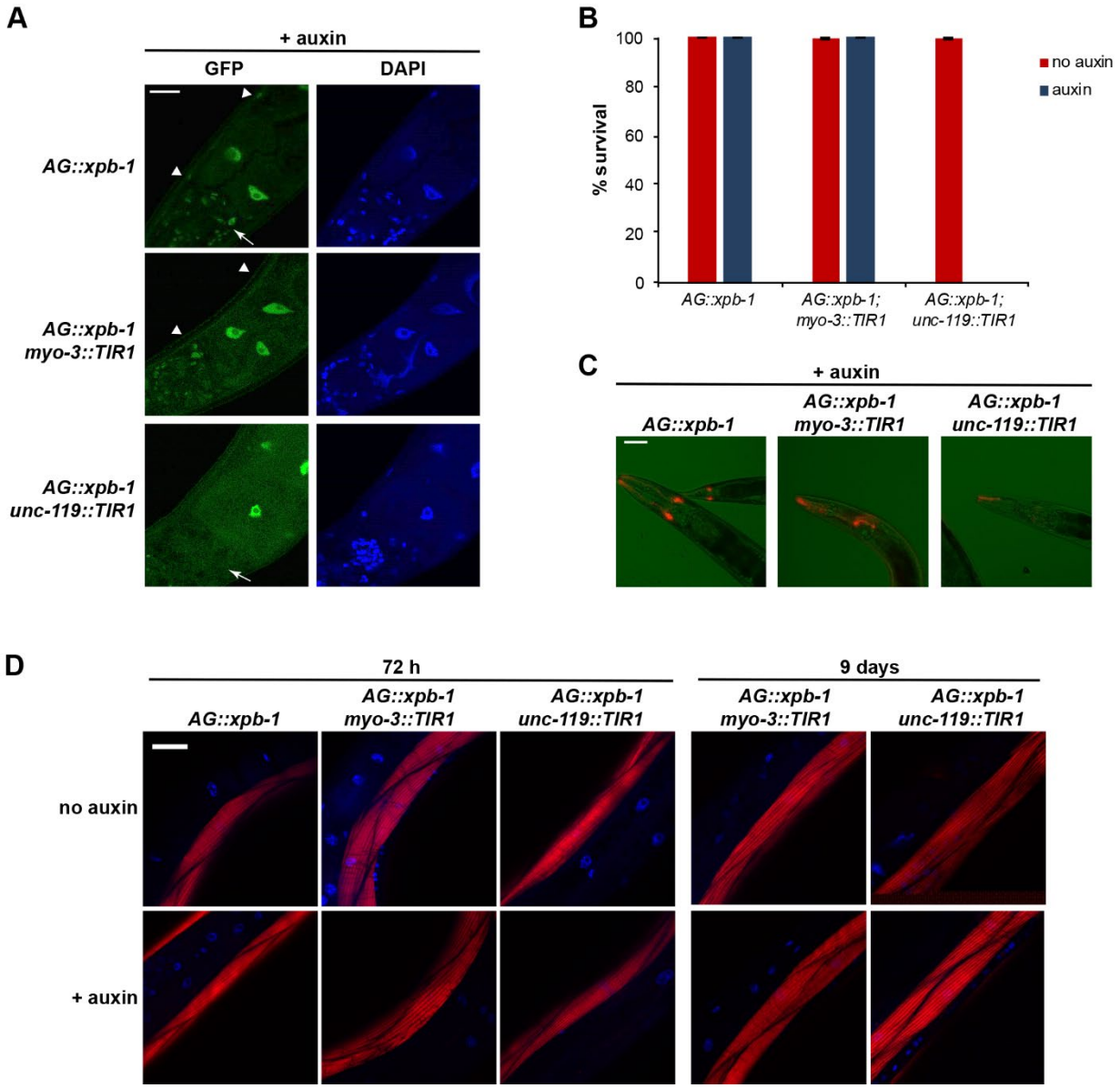

Figure S3. Neuron-specific transcription inhibition by XPB-1 depletion impairs neuron integrity and larval development. Related to Figures 2 and 6. (A) AID::GFP::XPB-1 fluorescence in wild type *xpb-1* knock-in animals (*AG::xpb-1)* or knock-in animals expressing TIR1 specifically in muscles (*AG::xpb-1; myo-3::TIR1*) or neurons (*AG::xpb-1; unc-119::TIR1)* grown for 72 h on plates containing 1 mM auxin. Muscle cell nuclei are indicated by arrow heads, neuron nuclei are indicated by arrows. Scale bar: 20 µm (B) L1 larvae survival assay of *AG::xpb-1, AG::xpb-1; myo-3::TIR1 and AG::xpb-1; unc-119::TIR1* animals grown for 48 h on plates with no auxin or with 1 mM auxin added. The percentages of animals that developed beyond the L2 stage (survival) are plotted, as average of three replicate experiments. Error bars represent the SEM. (C) DiI dye filling of *AG::xpb-1, AG::xpb-1; myo-3::TIR1 and AG::xpb-1; unc-119::TIR1* adult animals grown for 7 days on plates containing 1 mM auxin. The merge of the bright field and DiI (red) channel is shown. Scale bar: 50 µm (D) Phalloidin staining (red) of body wall muscles of *AG::xpb-1, AG::xpb-1; myo-3::TIR1 and AG::xpb-1; unc-119::TIR1* adult animals grown for 72 h or 9 days in the absence or presence of 1 mM auxin. DNA is stained with DAPI (blue). Scale bar: 20 µm

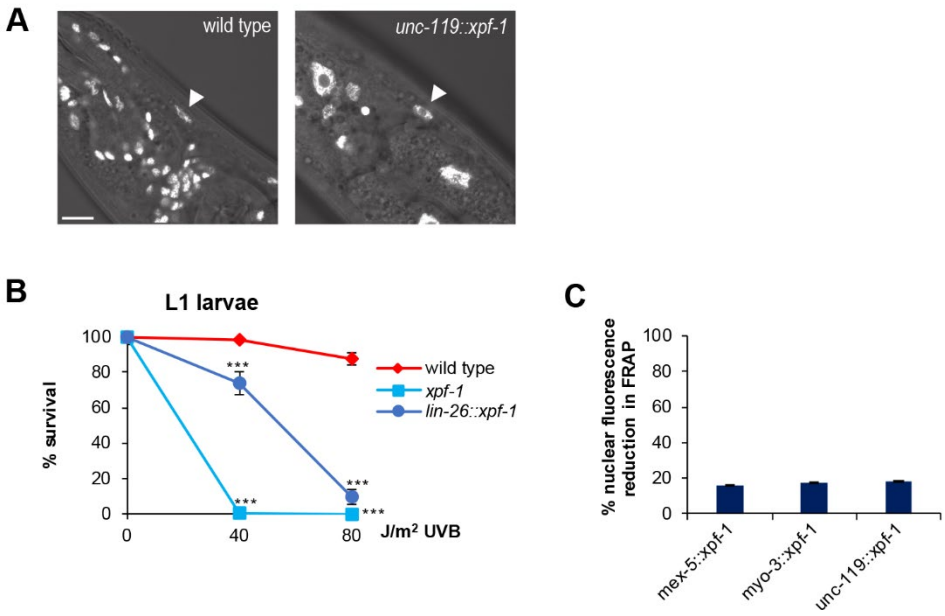

Figure S4. Intact muscle cells after UV and XPF-1 partially protects against UV in hypodermis. Related to Figures 5 and 6. (A) Representative images of body wall muscle cells (indicated by arrow heads) in adult wild type and *unc-119::xpf-1* animals, 72 h after UV irradiation (40 J/m^2) of L1 larvae. Shown are confocal bright field images overlaid with images of DAPI-colored nuclei (in white). Scale bar: 10 µm. (B) L1 larvae survival assay after UVB irradiation of wild type and *xpf-1* L1 larvae and L1 larvae transiently expressing XPF-1::GFP under the control of the *lin-26* (hypodermis) promoter. The percentages of animals that developed beyond the L2 stage (survival) after irradiation are plotted against the applied UVB doses. Results are plotted as average of eight independent experiments, normalized to untreated conditions. (C) Reduction in overall XPF::GFP fluorescence signal after photobleaching in a small square during FRAP experiments shown in Fig 6 in nuclei of oocytes of mex-5::xpf-1, of body wall muscle cells of *myo-3::xpf-1* and of ventral cord neurons of *unc-119::xpf-1* animals. Error bars represent the SEM. ***P<0.001 (one-way ANOVA followed by post-hoc analysis by Bonferroni's test) indicates statistically significant difference compared to wild type for each dose.

Table S1: *C. elegans* strains used in this study, as described in the STAR methods.

Strain	Genotype
CA1202	*ieSi57 [P(eft-3)::TIR1::mRuby] II; ieSi58 [P(eft-3)::AID::GFP] IV*
EG6250	*unc-119(ed3) III; cxTi10882 IV*
GJ1564	*xpf-1(tm2842) II*
GJ1519	*csb-1(ok2335) X*
GJ1553	*xpc-1(tm3886) IV*
HAL20	*xpf-1(tm2842) II; emcSi7[P(mex-5)::xpf-1::GFP] IV*
HAL21	*ercc-1(tm 2073) I; xpf-1(tm2842) II; emcSi7[P(mex-5)::xpf-1::GFP] IV*
HAL42	*xpf-1(tm2842) II; xpc-1(tm3886) emcSi7[P(mex-5)::xpf-1::GFP] IV; itIs37[P(pie-1)::mCherry::H2B]*
HAL43	*xpf-1(tm2842) II; emcSi7[P(mex-5)::xpf-1::GFP] IV; itIs37[P(pie-1):: mCherry::H2B]; csb-1(ok2335) X*
HAL44	*xpf-1(tm2842) II; emcSi7[P(mex-5)::xpf-1::GFP] IV; itIs37[P(pie-1):: mCherry::H2B]*
HAL62	*xpf-1(tm2842) II; emcSi24[P(myo-3)::xpf-1::GFP] IV*
HAL63	*xpf-1(tm2842) II; emcSi27[P(unc-119)::xpf-1::GFP] IV*
HAL69	*xpf-1(tm2842) II; emcEx42[P(aex-3)::xpf-1::GFP P(myo-3)::mCherry]*
HAL75	*xpf-1(tm2842) II; emcEx48[P(lin-26)::xpf-1::GFP P(myo-2)::mCherry P(elt-2)::mCherry]*
HAL77	*xpf-1(tm2842) II; emcEx50[P(hlh-1)::xpf-1::GFP P(myo-2)::mCherry P(elt-2)::mCherry]*
HAL100	*emcSi57[xpf-1::GFP] II*
HAL128	*xpf-1(tm2842) II; emcSi27[P(unc-119)::xpf-1::GFP]IV; csb-1(ok2335) X*
HAL130	*xpf-1(tm2842) II; xpc-1(tm3886) emcSi27[P(unc-119)::xpf-1::GFP] IV*
HAL204	*emcSi58[AID::GFP::xpb-1] III*
HAL228	*emcSi58[AID::GFP::xpb-1] III; emcSi70[P(unc-119)::TIR1::mRuby] IV*
HAL233	*emcSi58[AID::GFP::xpb-1] III; emcSi71[P(myo-3)::TIR1::mRuby] IV*
HAL246	*emcSi77[xpf-1::AID::GFP] II*
HAL247	*emcSi77[xpf-1::AID::GFP] II; emcSi70[P(unc-119)::TIR::mRuby] IV*
HAL248	*emcSi77[xpf-1::AID::GFP] II; emcSi71[P(myo-3)::TIR::mRuby] IV*
HAL250	*reSi3 [P(unc-54)::TIR1::F2A::mTagBFP2::NLS::AID I; emcSi77[xpf-1::AID::GFP] II*
HAL252	*reSi7 [P(rgef-1)::TIR1::F2A::mTagBFP2::NLS::AID] I; emcSi77[xpf-1::AID::GFP] II*
HAL253	*xpf-1(tm2842) ieSi57[P([eft-3)::TIR1::mRuby] II; ieSi58 [P(eft-3)::AID::GFP] IV*
HCL67	*uocIs1[P(eft-3)::Cas9 dpiRNA] II; unc-119(ed3) III*